



## RESEARCH ARTICLE

10.1002/2016JB013458

## Key Points:

- GPS Imaging is a new technique that provides a temporally and spatially robust vertical velocity field for geodynamic studies
- The Sierra Nevada is the most rapid and extensive uplift feature in the western United States, rising up to 2 mm/yr
- Images of an uplift discontinuity suggest that current rise of the Sierra Nevada is associated with evolution of the southern Walker Lane

## Supporting Information:

- Table S1

## Correspondence to:

W. C. Hammond,  
whammond@unr.edu

## Citation:

Hammond, W. C., G. Blewitt, and C. Kreemer (2016), GPS Imaging of vertical land motion in California and Nevada: Implications for Sierra Nevada uplift, *J. Geophys. Res. Solid Earth*, 121, doi:10.1002/2016JB013458.

Received 11 AUG 2016

Accepted 10 OCT 2016

Accepted article online 12 OCT 2016

## GPS Imaging of vertical land motion in California and Nevada: Implications for Sierra Nevada uplift

William C. Hammond<sup>1</sup>, Geoffrey Blewitt<sup>1</sup>, and Corné Kreemer<sup>1</sup>

<sup>1</sup>Nevada Geodetic Laboratory, Nevada Bureau of Mines and Geology, University of Nevada, Reno, Reno, Nevada, USA

**Abstract** We introduce Global Positioning System (GPS) Imaging, a new technique for robust estimation of the vertical velocity field of the Earth's surface, and apply it to the Sierra Nevada Mountain range in the western United States. Starting with vertical position time series from Global Positioning System (GPS) stations, we first estimate vertical velocities using the MIDAS robust trend estimator, which is insensitive to undocumented steps, outliers, seasonality, and heteroscedasticity. Using the Delaunay triangulation of station locations, we then apply a weighted median spatial filter to remove velocity outliers and enhance signals common to multiple stations. Finally, we interpolate the data using weighted median estimation on a grid. The resulting velocity field is temporally and spatially robust and edges in the field remain sharp. Results from data spanning 5–20 years show that the Sierra Nevada is the most rapid and extensive uplift feature in the western United States, rising up to 2 mm/yr along most of the range. The uplift is juxtaposed against domains of subsidence attributable to groundwater withdrawal in California's Central Valley. The uplift boundary is consistently stationary, although uplift is faster over the 2011–2016 period of drought. Uplift patterns are consistent with groundwater extraction and concomitant elastic bedrock uplift, plus slower background tectonic uplift. A discontinuity in the velocity field across the southeastern edge of the Sierra Nevada reveals a contrast in lithospheric strength, suggesting a relationship between late Cenozoic uplift of the southern Sierra Nevada and evolution of the southern Walker Lane.

### 1. Introduction

Steady contemporary vertical motion of the solid Earth is a consequence of ongoing geologic, volcanic, and geodynamic processes. Measurement of these motions reveals how the Earth behaves under various loads, provides information about the source and magnitude of forcings, and can be used to estimate the Earth's material and rheological properties. Multiple long-lived processes drive these motions. For example, glacial isostatic adjustment (GIA) drives continent-scale vertical land motion whose rates and patterns constrain mantle viscosity [e.g., Peltier, 1998; Milne et al., 2001; Sella et al., 2007; Tamisiea and Mitrovica, 2011] and has important implications for relative sea level rise that can impact coastal communities [Conrad, 2013; Hamlington et al., 2016; Wöppelmann and Marcos, 2016]. Postseismic uplift following large earthquakes provides critical complementary constraints on crustal and mantle viscosity, porosity, and fault frictional properties [e.g., Pollitz et al., 2001; Fialko, 2004; Gorumelen and Amelung, 2005; Freed et al., 2007; Bürgmann and Dresen, 2008; Hammond et al., 2009; Barbot et al., 2009]. The pattern and rate of elastic uplift from strain accumulation on faults, especially along Earth's subduction zones, constrain the distribution and degree of locking of the fault and constrain seismic and tsunami potential [Aoki and Scholz, 2003; McCaffrey et al., 2007; Burgette et al., 2009].

Although mountains may rise in response to tectonics, the contemporary geodetic signal can be overprinted by larger or shorter-lived signals that need to be understood and removed before background tectonics are revealed [e.g., Bürgmann et al., 2006; Beavan et al., 2010; Ching et al., 2011]. Less steady processes include coseismic fault slip, rapid postseismic deformation, groundwater subsidence, magmatic inflation, and hydrological loading. One recent example is the observation that vertical motions in the western United States can be attributed to seasonal to decadal changes in terrestrial water storage [Amos et al., 2014; Borsa et al., 2014; Fu et al., 2014; Argus et al., 2014]. Similarly, in combination with other measurements, movement of magma can be located and tracked using vertical surface motion [Dzurisin et al., 1991; Fialko et al., 2001; Wicks et al., 2002; Feng and Newman, 2009; Liu et al., 2011].

Owing to measurement challenges, comprehensive models of the vertical velocity field analogous to strain rate maps of horizontal motion [e.g., Haines and Holt, 1993; Kreemer et al., 2014] have been difficult to obtain.

©2016. The Authors.

This is an open access article under the terms of the Creative Commons Attribution-NonCommercial-NoDerivs License, which permits use and distribution in any medium, provided the original work is properly cited, the use is non-commercial and no modifications or adaptations are made.

This is largely because vertical velocity magnitudes tend to be smaller (measured in mm/yr, compared to cm/yr for horizontal rates), have greater noise and systematic error, and do not cumulatively increase across domains such as tectonic plate boundary zones. Furthermore, the impact of nonlinearity in the vertical component time series, isolated disturbances on sensitive Global Positioning System (GPS) instrumentation, or ground motion very local to GPS stations have been difficult to remove systematically and objectively. However, recent continued expansion of GPS networks in the western U.S. is providing unprecedented quantities of data to mitigate the observation noise.

Here we present a new analysis method called GPS Imaging that uses robust and unbiased estimation to cope with noise and uncertainty to enhance the signals of flex and flow in the solid Earth. This result is a stable interpolation of the data that leads to better visualization and interpretation, with greater impact and utility for geodynamic investigations. We use as input velocities obtained with the recently developed MIDAS trend estimator that reduces the impact of seasonality, undocumented steps, and outliers in the position time series [Blewitt *et al.*, 2016]. We then apply similar principles to the spatial part of the estimation, defining a method for filtering and interpolation similar in spirit to geostatistical kriging analysis [Krig, 1951; Matheron, 1963]. However, GPS Imaging differs from traditional kriging in key aspects; in that, it does not use least squares to formulate the spatial dependence and uses weighted medians to make estimates at the evaluation points that are insensitive to isolated outliers. The use of median statistics in both the temporal and spatial domains ensures that GPS Imaging produces a velocity field that reflects trends in the majority of the data, while tolerating potentially major problems in the data that may be either transient or localized in nature. The technique is computationally efficient, allowing integration of thousands of stations, a necessary feature in the context of GPS networks experiencing exponential growth.

Finally, we apply GPS Imaging to assess the uplift signals across California and Nevada, western United States, and focusing on uplift of Sierra Nevada range (Figure 1). Previous analyses and interpretations of vertical GPS time series in Southern California [e.g., Tape *et al.*, 2009; Marshall *et al.*, 2013] and southern Sierra Nevada [Fay *et al.*, 2008; Bennett *et al.*, 2009] have recognized the challenges in resolving the vertical GPS velocities, finding patterns, and assigning them to physical processes. Here we extend our previous plate boundary-scale analyses [Hammond *et al.*, 2012; Amos *et al.*, 2014] to place the Sierra Nevada uplift into tectonic context and use the results to argue that a contrast in lithospheric strength at the southeastern edge of the Sierra Nevada/Central Valley (SNCV) microplate is related to late Cenozoic uplift of the southern Sierra.

## 2. GPS Data

### 2.1. GPS Networks

We use data from GPS networks distributed throughout California and Nevada that are heterogeneous in their history and operation, although all have stable monuments and provide daily receiver-independent exchange observation files. We considered data available between years 1996.0 and 2016.1 from continuous networks (see Acknowledgments section). Additionally, we use data from the semicontinuous MAGNET GPS network operated by the University of Nevada, Reno [Blewitt *et al.*, 2009]. In most cases we only used a station if it has a time series of at least 5 year duration and lies within the latitude/longitude bounds shown in Figure 1. The archives from which we downloaded data are given in Table S1 in the supporting information.

### 2.2. GPS Data Processing

GPS data were processed using the GPS Inferred Positioning System (GIPSY) OASIS II software made available by the Jet Propulsion Laboratory (JPL) and using their final fiducial-free GPS orbit products [Bertiger *et al.*, 2010]. The precise point positioning method was applied to ionospheric-free carrier phase and pseudorange data [Zumberge *et al.*, 1997]. All models and conventions used in the processing are documented at our data center (<http://geodesy.unr.edu/>), which we do not repeat here as the sequence has been described elsewhere [Blewitt *et al.*, 2013]. All daily 24 h solutions are aligned from a global reference frame (from the International GNSS Service 2008 (IGS08)) to a North America fixed reference frame (NA12) that is constructed to have zero net vertical axis rotation with respect to the rigid interior of the North American continent [Blewitt *et al.*, 2013]. The daily alignments include scale transformation which provides a continent-wide regional filtering that suppresses common-mode noise [Wdowinski *et al.*, 1997], reducing scatter in the vertical coordinate time series while preserving signals from local to regional deformation. An effect of this kind of filtering is that if rates change uniformly over the entire network after the time of frame construction, the

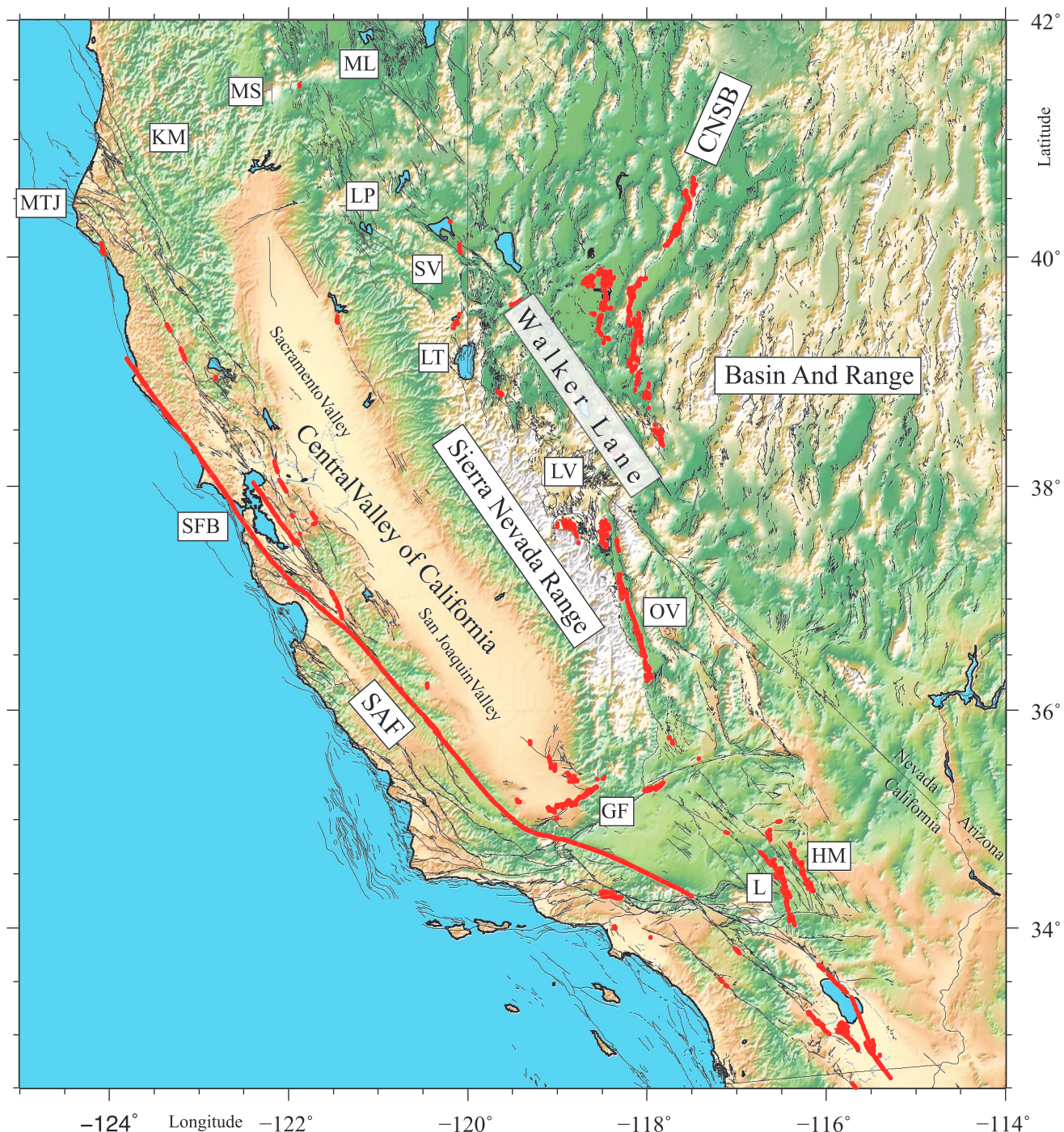


**Figure 1.** The color-shaded topography of study region including the western U.S. states of California and Nevada. Historic surface ruptures including those of the Central Nevada Seismic Belt (CNSB), San Andreas Fault (SAF), Owens Valley (OV), Hector Mine (HM), and Landers (L) are shown with red lines. Location of volcanic centers are annotated as ML = Medicine Lake, MS = Mount Shasta, LP = Lassen Peak, and LV = Long Valley. Other locations are MTJ = Mendocino Triple Junction, SFB = San Francisco Bay Area, KM = Klamath Mountains, LT = Lake Tahoe, SV = Sierraville, and GF = Garlock Fault.

changes will be suppressed. As previously shown by *Borsa et al.* [2014] and discussed below, vertical rates increased across the western U.S. interior owing to drought after 2012, but this area is small compared to the size of the NA12 filtering domain [*Blewitt et al.*, 2013] so the impact is small. However, it could contribute to the median difference between IGS08 and NA12 vertical rates ( $\sim 0.67 \text{ mm/yr}$  with IGS08 giving faster uplift), which is near the accuracy limit of the connection of the global frame origin to Earth center of mass [Altamimi

*et al.*, 2011]. We use the NA12 rates because filtering increases resolution of relative vertical rates across the study area, although it may cause a small increase uncertainty of the median rate of the entire network to the Earth center of mass. All the resulting time series from which we derived velocities are available online via our data product portal at <http://geodesy.unr.edu>.

### 2.3. MIDAS Vertical Velocities

The station velocities used as input to this analysis are obtained by applying the MIDAS algorithm [Blewitt *et al.*, 2016] to the vertical coordinate time series. The algorithm is a variant of the Theil-Sen nonparametric median trend estimator [Theil, 1950; Sen, 1968], modified to use pairs of data in the time series separated by approximately 1 year, making it insensitive to seasonal variation and time series outliers. The MIDAS-estimated velocity is essentially the median of the distribution of these ~1 year slopes, making it insensitive to the effects of steps in the time series (even if they are undocumented and occur at unknown epochs) if they are sufficiently infrequent. It is robust and unbiased, making it desirable for the estimation of vertical component trends. MIDAS provides uncertainties based on the scaled median of absolute deviations of the residual dispersion, and thus, velocity uncertainties increase if the time series have more scatter or are less linear. The uncertainties have been shown to be realistic and usually do not require further scaling. In blind tests using synthetic data with unknown step functions inserted, MIDAS outperformed all 20 other automatic algorithms tested in terms of the 5th percentile range of accuracy [Blewitt *et al.*, 2016]. Files with MIDAS velocities are now available online (<http://geodesy.unr.edu>) and are recomputed each week to account for new data at all stations processed at the Nevada Geodetic Laboratory.

To ensure that we are using only the highest-quality velocity data we omit any station from consideration if the MIDAS vertical velocity uncertainty is greater than 5 mm/yr or if the time series duration is less than 5 years. In all we use vertical velocities for 1232 stations. Histograms of the vertical velocities for stations within the bounds of Figure 1 and their MIDAS uncertainties are shown in Figure 2 and are provided in Table S1. Vertical velocities have a median near zero; 86% are between –2 and 2 mm/yr, and 92% are between –3 and 3 mm/yr. The horizontal axis in Figure 2a has been truncated to focus on the largest portion of the data; the maximum velocity is 7.3 mm/yr and the minimum is –299 mm/yr. This rapidly dropping station (CRCN) is in an agricultural area of the San Joaquin Valley (SJV) near Visalia, California. It is likely affected by shallow and/or groundwater hydrological effects and is an example of an outlier in the velocity field. Similar to least squares estimation, the uncertainty in vertical velocity decreases with the length of the position time series (Figure 2c), with 81% of the velocity having uncertainties less than 1.0 mm/yr with a median uncertainty of 0.6 mm/yr. Vertical velocities are shown in map view in Figure 3a.

## 3. Analysis: The GPS Imaging Method

The technique we describe here may best be described as a hybrid between geostatistical field estimation from sample point data known as kriging [Krige, 1951; Matheron, 1963] and image-processing techniques that enhance and repair signals on more spatially complete image data. Our method combines some of the strengths that kriging brings to interpolation, in particular the introduction of a spatial structure function that represents the variability of the data as a function of distance between stations. However, our method differs in key ways; e.g., kriging is generally based on the minimization of the sum of squared prediction errors, while our method uses weighted medians to estimate values inside local clusters of nearby stations. GPS Imaging estimated values are not based on a weighted sum of all the data, rather only on the nearest stations. While some kriging variants incorporate medians into construction of a more robust spatial mean field, notably median polish kriging [Cressie, 1990] and modified median polish kriging [Berke, 2001], they still essentially decompose the data into deterministic and stochastic components via the kriging formalism and estimate values based on weighted sums of all data. GPS Imaging, like imaging processing, does not draw on the theory of random fields. Instead, the contribution to each grid point value only comes from the closest stations, i.e., those connected via a triangulation. This is an important property because it allows preservation of edges (sharp contrasts between human-recognizable domains) in the velocity field when station density is sufficient to resolve them. Edges, i.e., sharp quasi-linear transitions in the field, may be present at creeping faults or at broken plates, so we require that estimation be supported by multiple stations while being as local as possible.

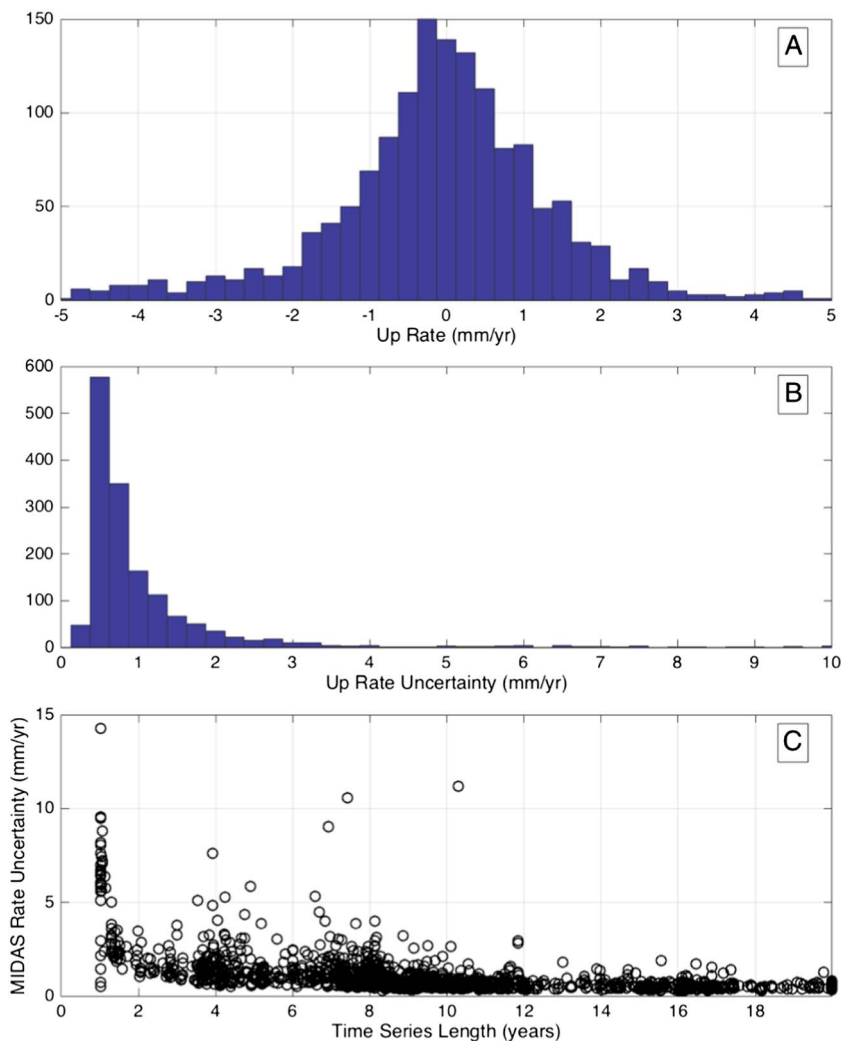


**Figure 2.** (a) Histogram of MIDAS GPS vertical velocities in California and Nevada. (b) Histogram of MIDAS uncertainty in vertical GPS velocity. (c) MIDAS vertical velocity uncertainty as a function of the length of GPS time series.

GPS Imaging is designed to work well when (1) there are a lot of data, (2) signal-to-noise ratio  $s$  are low, (3) station density is highly heterogeneous, (4) the structure of the underlying signal is unknown, and (5) outliers in the field are agreed to be “noise.” In these cases GPS Imaging works better than commonly used interpolation schemes. For example, spline coefficients derived through least squares estimation can be distorted by outliers, speckles, or discontinuities in the field or poorly constrained when station density is highly heterogeneous, making polynomial coefficients of fixed order on a predefined grid difficult to estimate.

### 3.1. Spatial Structure Function

Analogous to kriging we require a spatial structure function  $ssf$  to contain the information representing the variance of the signal that is attributable to the distance between stations. Stations far from one another are more likely to move independently from one another than stations close to one another. How rapidly the variance of vertical velocity between pairs of stations falls off with distance between stations depends on the underlying spatial wavelength of the signals in the data. Some locations on Earth have very long wavelength vertical signals. For example, GIA in northern North America has vertical velocities that may be correlated over  $10^3$  to  $10^4$  km owing to the extensive load and deep mantle response of the rebound. Conversely, at other locations such as Southern California, the correlations may be poor over much shorter distances, where vertical velocity varies across aquifers and fault systems separated only by  $10^0$  to  $10^2$  km.

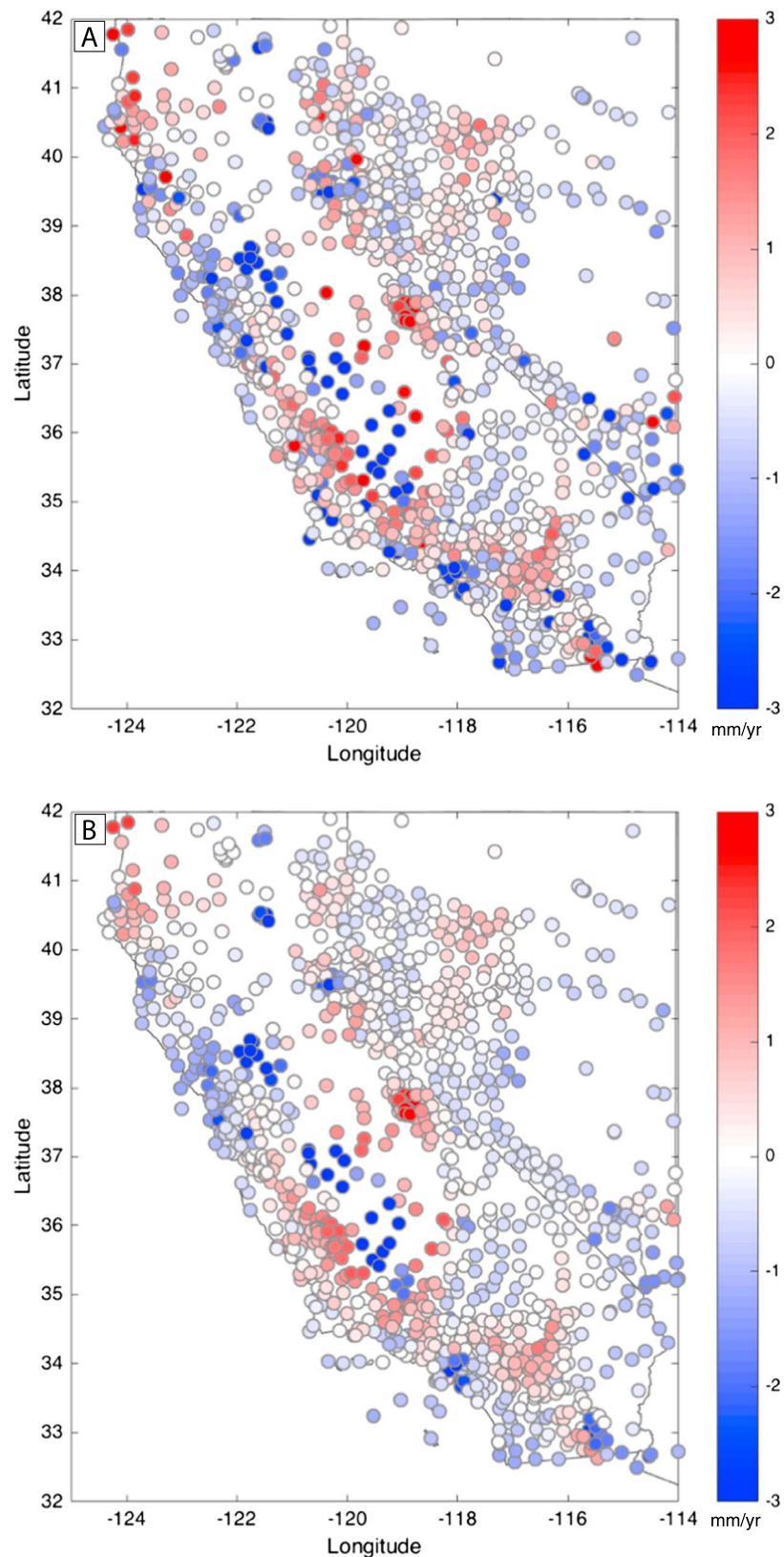


**Figure 3.** (a) MIDAS vertical GPS velocities for all stations with over 5 year time series duration, in the NA12 reference frame [Blewitt et al., 2013]. (b) MIDAS velocities with median spatial filter applied. The color scale is in mm/yr; positive (red) is upward, and negative (blue) is downward. The color scale in both plots is in mm/yr.

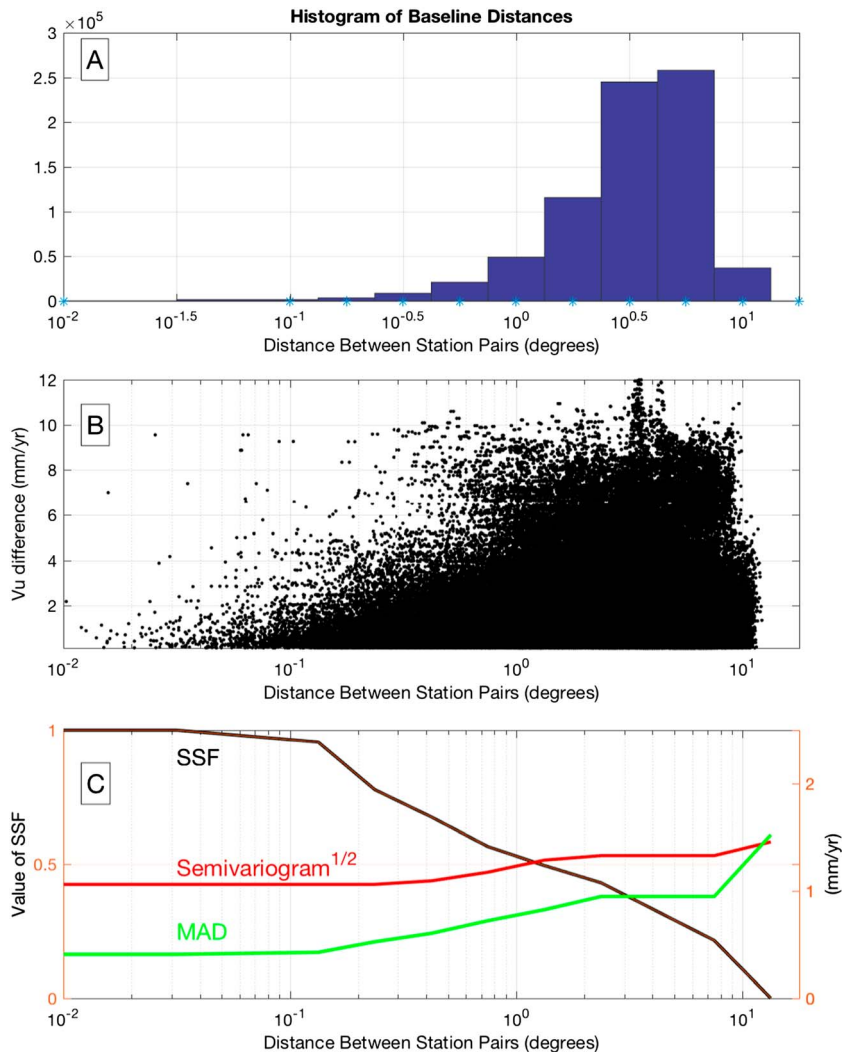


**Figure 4.** Construction of the spatial structure function (*ssf*) that defines the part of the weight in equation (3) that is a function of distance between GPS stations and an evaluation point. (a) Histogram of the distances between pairs of GPS stations in California and Nevada. (b) Absolute value of difference in vertical GPS velocity as a function of baseline distance. (c) Value of *ssf* as function of distance (black line—left vertical axis) derived via the MAD of data in bins of data in Figure 4b (green line—right vertical axis; see text for explanation). For comparison, the semivariogram discussed in kriging literature is shown (red line—right vertical axis).

To address this, we develop an empirical *ssf* that is tuned to our problem from the data in our domain of interest (Figure 1). The similarity of signal as a function of great circle distance in degrees ( $\Delta$ ) is estimated from the vertical GPS velocity data. We define the *ssf* to have value 1 at  $\Delta=0$  with the property that it is forced to decrease monotonically to zero with distance in the far field ( $\Delta=\infty$ ). As a practicality we force the function to be zero at a distance similar to the maximum dimension of our model domain, but this has little impact because the *ssf* is always employed for interstation distances much smaller than the size of the domain (there is no need for a *sill*). For every pair of stations we calculate the absolute value of the difference between vertical velocities  $\delta v$  and plot those differences as a function of  $\log_{10}(\Delta)$  (Figure 4b). Following the theme of robustness in each stage of our analysis we calculate the median absolute deviation (MAD) of the absolute velocity differences inside bins of  $0.25 \log_{10}(\Delta)$  units. We force this function (green line in Figure 4c) to increase monotonically with baseline distance by sequentially, over increasing  $\Delta$ , assigning the value for each bin to be the maximum of the value in the bin  $k$  and the previous bin  $k-1$ . For comparison to a function commonly used in kriging we plot (red line in Figure 4c) the square root of the empirical semivariogram, which is defined as one half of the mean square of the velocity differences as a function of  $\Delta$  [Matheron, 1963]. The

semivariogram will be more sensitive to outliers since it is based on the squared differences, explaining why the MAD-based function has a steeper slope. To obtain the *ssf* we invert the MAD-based function

$$\text{ssf}_0(\Delta_k) = 1 / \max([\text{MAD}(\delta v_{k-1}, \text{MAD}(\delta v_k))]) \quad (1)$$

and then normalize the function to that its maximum value is 1

$$\text{ssf}(\Delta_k) = \text{ssf}_0(\Delta_k) / \max(\text{ssf}_0(\Delta)). \quad (2)$$

Estimation of the *ssf* over very short distances is unstable because of the few number of pairs with very short baselines (Figure 4b). Additionally, the *ssf* must always be flattened near  $\Delta = 0$  since  $1/\delta v$  approaches infinity. Based on the binning we chose (responding to station density) and the assumption that the  $\text{ssf}(0) = 1$ , we set the first two points ( $\Delta \leq 3$  km) of the *ssf* to flat unity.

### 3.2. Median Spatial Filtering

In the second step we filter the velocities at the stations using an algorithm that replaces the velocity at each station with the weighted median of values of nearby stations. This filtering step reduces the influence of outlier values that are substantially different from neighboring rates. The filtering is accomplished by forming a Delaunay triangulation of the station locations on a sphere [Delaunay, 1934; Renka, 1997] and taking the weighted median of vertical velocities in the set of stations connected to the evaluation point (which is a station in this step). The Delaunay triangulation is useful because it connects the evaluation point to a small set of its nearest neighboring GPS sites, which keeps the contributing area as small as possible given the station density. Also, this triangulation is unique and reproducible; software to compute it is openly available, commonly used, and run with usually short execution time. Again, we use median values (as opposed to means), making the new value unbiased by outliers and improving robustness. The effect is similar to that of a despeckling filter that is commonly used in image-processing applications to restore damage to films, correct for artifacts, errors, or gaps introduced in generating or preserving the images [e.g., Castlemann, 1996].

Using a weighted median allows us to increase the importance of stations near the evaluation point and decrease the importance of stations with greater uncertainties. To compute the spatially filtered velocity  $u_j$  at the evaluation point  $j$  we build weights using the *ssf* constructed earlier, scaled by the contributing velocity uncertainties

$$w_i = \text{ssf}(\Delta_{k(i,j)}) / \sigma_i, \quad (3)$$

$$u_j = \text{weighted\_median}(v_i, w_i), \quad (4)$$

where the velocity uncertainties  $\sigma_i$  for the set of stations  $i$  that are connected to point  $j$  in the triangulation are used to obtain the weights  $w_i$ . The distance  $\Delta_{k(i,j)}$  refers to the bin  $k$  in equation (2) that contains the distance between the stations in pair  $(i, j)$ . The weighted median is calculated by sorting the elements and incrementally summing their normalized weighted values, taking the element reached prior to the sum exceeding 1/2 [Cormen et al., 2001]. To prevent zero length baselines in the Delaunay triangulation we first identify duplicate GPS station locations, and for any group that forms a cluster of 2 or more stations within 0.1 km of each other we take the median velocity and coordinates, and this velocity is assigned to a single station that represents the group. The median spatial filtered velocities in Figure 3b were obtained by applying the filter where the evaluation points are the locations of the GPS stations. An example of a particular estimate near the Southern California coast is shown in Figure 5.

Given the distribution of weights and Delaunay connectivity it is possible that the importance of the velocity value at a station will be less than that of the combined influence of the other stations. In these cases, the field can become excessively smooth. Since part of our purpose is to preserve edges in the velocity field, we provide a mechanism to override the value of weighting at zero distance from the evaluation point, so the user can increase the weight of the local station. This only has an effect during this first filtering step. It has almost no effect in the imaging step discussed below, when evaluation points are usually not zero distance from the nearest station. In the filtered velocities presented in Figure 3b we include a self-weight of 0.5.

### 3.3. Imaging

In the third step we perform the imaging, where we apply the algorithm with the filtered velocities as input and where evaluation points are locations on a regular grid with spacing of 0.05° in both longitude and

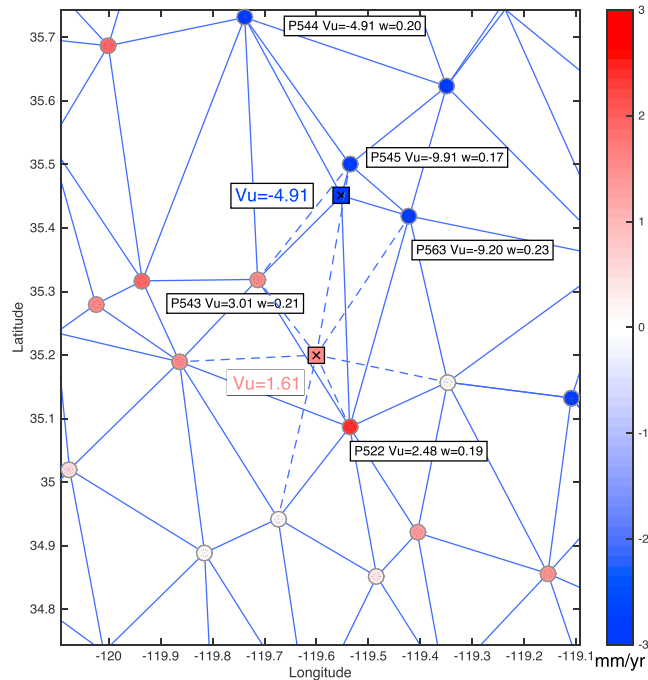


**Figure 5.** Illustration of vertical velocity estimated from GPS stations (circles) at two locations near boundary between Great Valley and Coast Ranges in central California (squares with crosses). GPS stations are colored by their vertical rate according to the color scale on the right (mm/yr). Connections of the Delaunay triangulation are shown with the blue lines, dashed where triangulation is different for more southern square. The estimate of vertical rate is the weighted median of values at connected stations, with station names, values ( $V_u$ ), and weights ( $w$ ) shown for stations connected to the more northern square.

tainties in the contributing rates, reduced approximately by a factor of  $N^{-1/2}$ . However, this does not account for the limitation of the model which leaves a residual scatter among contributing velocities that can be larger in areas where the GPS velocities vary rapidly across locations.

To understand the different components of uncertainty we estimate it in two ways. The first method computes the uncertainty in the weighted mean of the contributing rates (Figure 7a), and the second method computes the root-mean-square residual scatter of the contributing values (Figure 7b). The median uncertainty in the first method is 0.30 mm/yr, whereas the median uncertainty using the second method (accounting for scatter) is approximately 3 times as large, 1.00 mm/yr. The scatter-based uncertainties are larger where signals vary rapidly with location, such as across the California Central Valley and at the volcanic zones such as Mt. Lassen and Long Valley. In the second method the uncertainties are likely overestimated because the imaging method may be correctly interpolating between neighboring rates and thus are accurate even though neighboring rates differ. The formal uncertainties in the first method may be underestimated but closer to accurate since several signals near 1 mm/yr, such as the uplift at the Central Nevada Seismic Belt, are similar to the predictions of postseismic viscoelastic relaxation models [Gourmelen and Amelung, 2005; Hammond et al., 2012], and thus appear to be reliably imaged. These two estimates represent realistic lower and upper bounds of uncertainty in the vertical rate field.

### 3.5. Checkerboard Test

The ability of a GPS network to resolve geographic variation in vertical velocities is important because these variations may have geodynamic significance. For example, the eastern perimeter of the Sierra Nevada uplift signal coincides with the eastern boundary of the Sierra Nevada/Central Valley microplate and western boundary of the Great Basin (Figure 6a). This geographically persistent edge in the velocity field separates upward motion of the Sierra Nevada from stable to slightly downward movement in the Walker Lane and

latitude directions (Figure 6a). In fact, the second step is optional and can be skipped since it is possible to apply the imaging step on the unfiltered data. This results, however, in an interpolated field that is clearly more sensitive to velocities that differ from the spatially variable robust field (Figure 6b), showing spots of up and down at individual stations that sometime change sign from station to adjacent station. In the interest of solving for a field more representative of geodynamic processes we prefer to interpret the filtered field in Figure 6a.

### 3.4. Uncertainty in the Vertical Velocity Field

Uncertainty in the derived velocity field is a function of the uncertainties of the individual GPS velocities, the distance from GPS stations to each evaluation point, and the interpolation process. Each pixel in the image is a weighted median of a set of nearby values that contribute to the estimate. As is the case for uncertainties in means, we expect the uncertainty in the weighted median to be less than the uncertainty

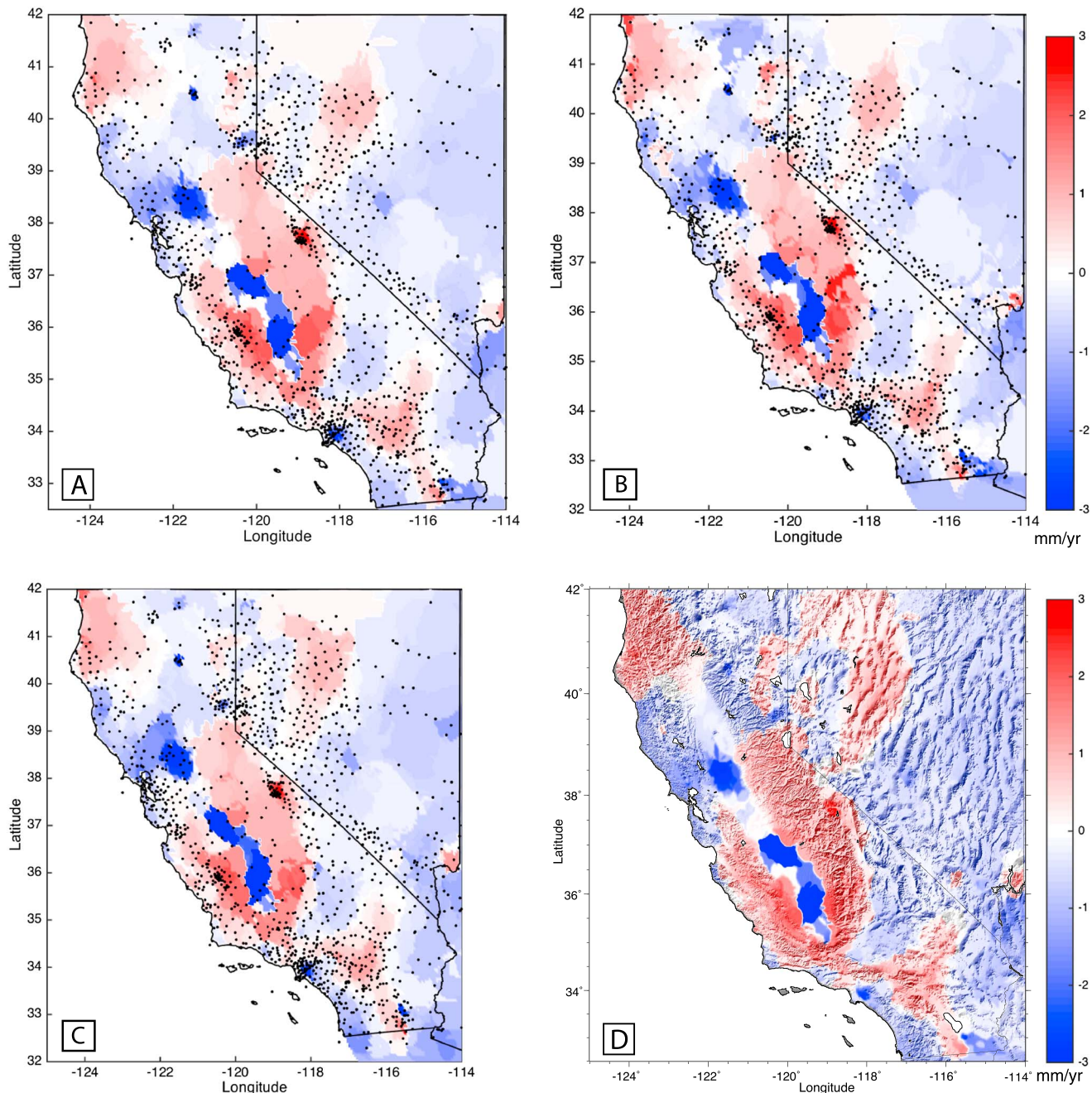


**Figure 6.** (a) Result of GPS Imaging of the vertical velocity field using the median spatial filtered MIDAS velocities. The black dots represent the GPS stations. The color scale is in mm/yr; positive (red) is upward, and negative (blue) is downward, saturated at color scale limits. (b) Result of GPS Imaging of the vertical velocity field on original MIDAS vertical velocities without preliminary median spatial filtering applied. The black dots represent the GPS stations. The color scale is in mm/yr; positive (red) is upward, and negative (blue) is downward. (c) Same as in Figure 6a except with a minimum time series duration cutoff of 2.5 years. (d) Same as in Figure 6a except that vertical rate is plotted over topography to illustrate correlation between imaging and geographic features.

Great Basin to the east. Before drawing conclusions about the significance of this transition we would like to know if this edge in this location and elsewhere in California and Nevada is resolvable given the distribution of GPS stations and the uncertainties in the individual observations.

We test the resolution of the network by employing a checkerboard test. We create a synthetic vertical velocity field by presuming  $1^\circ \times 1^\circ$  cells of alternating vertical velocity of  $\pm 3$  mm/yr, with a Gaussian smoothing applied so that the boundary area between cells has vertical velocity of 0 mm/yr (Figure 8a). We sample the velocity field at the location of the GPS stations (Figure 8b) and apply noise with standard deviation consistent with the

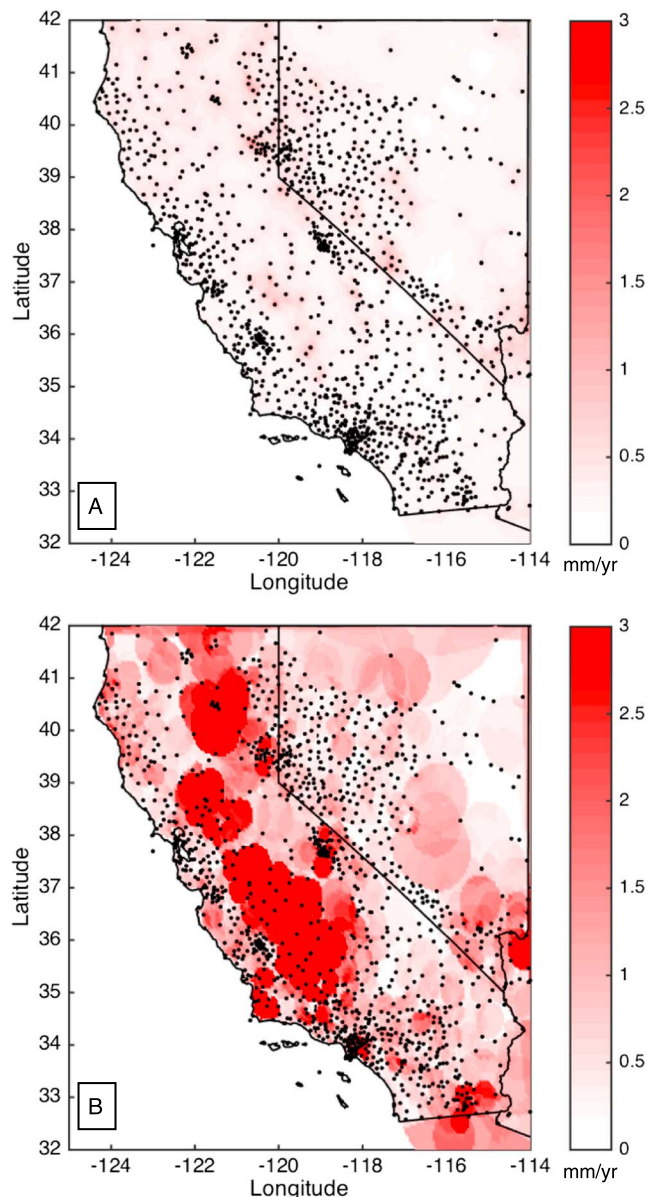


**Figure 7.** Uncertainty in image of vertical GPS velocity. (a) Formal uncertainty based on weighted mean of rates contributing to image estimate and (b) uncertainty based on residual scatter of contributing GPS rates.

are usually local and occur where station coverage is incomplete. However, where the GPS network has very low station density, e.g., in northeast Nevada, we see some disintegration of the structure. Clearly, these poorly resolved areas can be a target for future GPS network development.

#### 4. Uplift Over Time

Separation of the signal attributable to tectonic uplift of the Sierra Nevada Range from that of short-term response owing to loading from surface and groundwater is challenging. The contemporary response to which geodetic measurements are sensitive may be similar or different in velocity and/or spatial distribution to that of long-term tectonics [Fay *et al.*, 2008; Hammond *et al.*, 2012]. Hydrological mass loading signals vary over time with seasons, climate change, and extraction patterns but may be separable from long-term steady tectonic motion on that basis [Holzer, 1979; Fu and Freymueller, 2012; Argus *et al.*, 2014; Amos *et al.*, 2014; Borsa *et al.*, 2014].

MIDAS uncertainties in the velocity field. We apply GPS Imaging to this synthetic velocity field. The degree to which the result (Figures 8c and 8d) is similar to the original checkerboard is one measure of the ability of the data to accurately resolve sampled structures in the vertical GPS data. Since the final uncertainty has a contribution from both limitation of station distribution and uncertainty in the velocities, we also test the result when we assume that all velocity uncertainties are less than 1 mm/yr. This helps to isolate which parts of the failure to reconstruct the checkerboard are attributable to velocity uncertainty (and hence may be rectified once more data are collected in these stations) versus network weakness, where lack of GPS station coverage drives the uncertainty. Figure 8d also has a Gaussian smoothing similar to the input structure applied to illustrate the effect that smoothing has on reconstruction.

The resulting images overall show that in California/Nevada the  $1^\circ \times 1^\circ$  velocity cells are resolvable and return edge azimuths that are generally true to the starting model. Thus, the irregularity of the GPS station network is, to a degree, compensated for by the GPS Imaging method, and edges generally do not migrate or change azimuth over long distances. The peak amplitude of the returned structures are near or just below that of the input structures. Some wiggles and incompleteness of the cell boundaries are present, but these

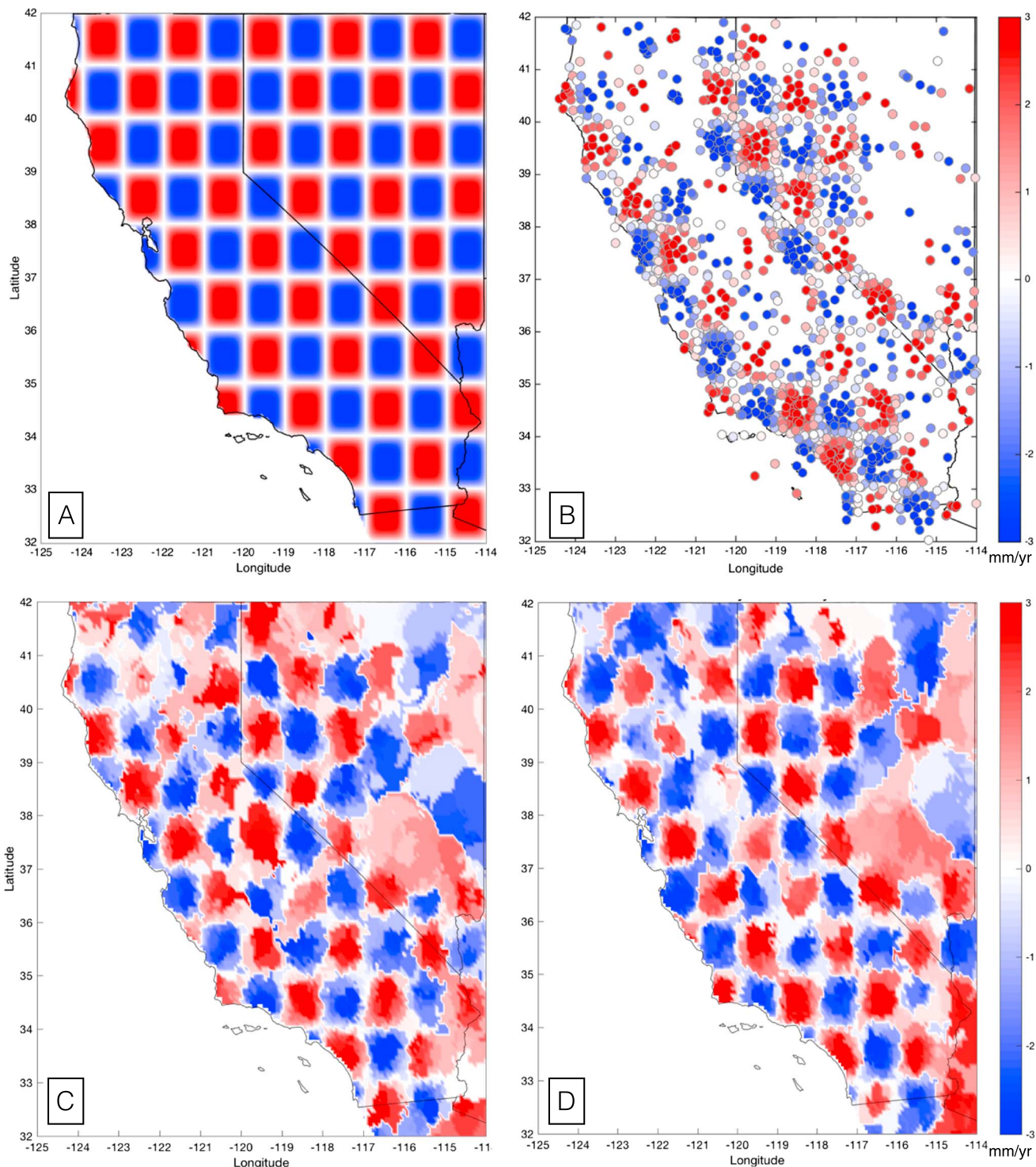


**Figure 8.** (a) Synthetic input checkerboard function of  $2^\circ \times 2^\circ$  grid with alternating positive and negative 3 mm/yr vertical velocities and (b) sampled at the GPS stations. The color scale is same as in previous figures. (c) Retrieved pattern of vertical rate applying GPS Imaging to the values at the stations in Figure 8b. (d) Result obtained assuming that time series are long enough and positioning noise is low enough to reduce all vertical velocity uncertainties to under 1 mm/yr.

GPS time series on the west slope of the Sierra Nevada show uplift that is generally not steady, decreasing in intensity from south to north along the range (examples in Figure 9). The winter of late 2010 to early 2011 had particularly heavy precipitation and was followed by 5 years of drought until late 2015. GPS vertical position time series show increased upward velocities during the drought period, suggesting a contribution from

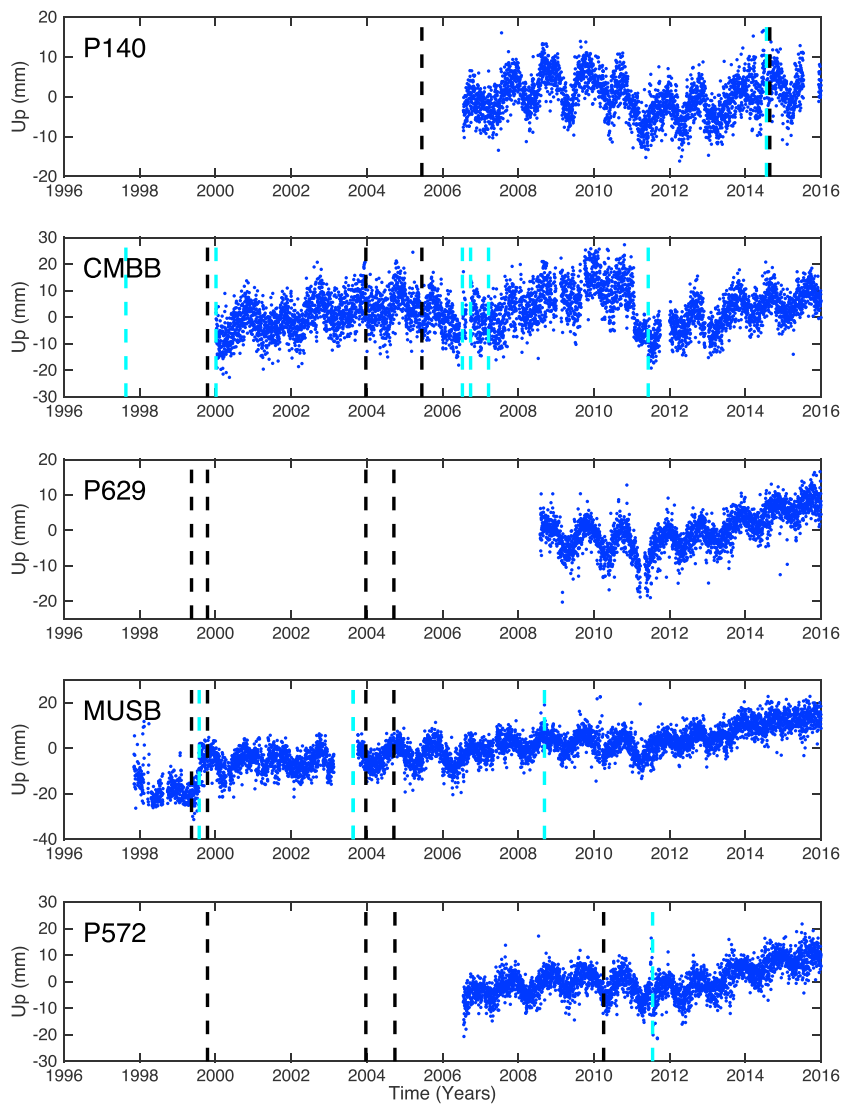


**Figure 9.** Time series of vertical GPS positions for stations on west slope of Sierra Nevada range, decreasing latitude from top to bottom. The black dashed lines indicate the times where some earthquake  $>M5.5$  occurred in the vicinity (but did not necessarily cause offset in vertical position). The cyan lines are the times of known GPS antenna or receiver change. For CMBB data before 2000.0 are not shown owing to large equipment-related step on time series.

nontectonic motion. However, we expect the signal of tectonic uplift to be constant over the time of observation. This does not necessarily imply that the signals would be upward during all times of drought. Some time series extend far enough into the past so it is clear that an upward trend existed before the drought interval (e.g., station MUSB; Figure 9). However, further in the past we have fewer GPS stations with 5 or greater year duration time series to estimate a robust vertical velocity (Figure 10) and is therefore more difficult to perform the imaging.

As a first attempt to resolve time variability of uplift, we apply GPS Imaging to two distinct, nonoverlapping time intervals. We find that imaging based on post-2010 data can create an uplift map similar to the image made using all data (Figure 11). However, using only pre-2010 data generates a poor image, where the reduced number and density of contributing GPS stations show some Sierra Nevada uplift but have difficulty constraining its geographic distribution. A better result is obtained when we divide the data at 2011.0. The later period's image is still similar to the image based on all data. Adding another year of data to the early period considerably improves the constraint on geographic distribution of uplift because more stations are available in the Central Valley and MAGNET GPS networks. Thus, the data set is capable of resolving two

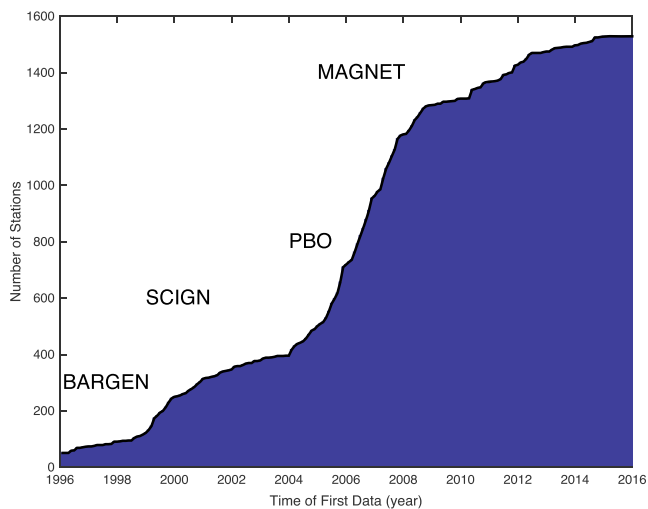


**Figure 10.** Cumulative number of California and Nevada continuous and semicontinuous GPS stations present in the Nevada Geodetic Laboratory database. Time of inception of a few networks are shown with annotation. The EarthScope Plate Boundary Observatory (PBO) was the single largest expansion of the number of precise continuous GPS stations.

future aquifers become completely depleted, then the signal of tectonic uplift will be modulated only by surface water mass changes. Or the southwest United States may fully emerge from drought and groundwater extraction rates may slow down, although aquifer levels will not be quickly restored. In either case data collection in continuous GPS networks will be critical in the future to determine whether accelerated uplift continues, slows, or reverses, providing an opportunity to better separate tectonic from nontectonic uplift.

## 5. Results and Discussion

Western U.S. GPS network distribution and density is highly variable, owing to its construction following diverse goals of scientific or societal interest. For example, some stations are deployed to monitor volcanoes, some for groundwater hydrology, some for province-wide tectonics, and some for surveying purposes. GPS Imaging is designed to perform well in this situation by providing an integrated synoptic view of vertical velocities attributable to all processes and constrained by all data. This enhances interpretation by placing all the signals into the same context. Here we interpret some of the uplift signals imaged in Figure 6a.

### 5.1. Volcanic Systems

Volcanic systems are an important feature in the vertical velocity images because they exhibit geographically focused signals, usually near the edifice. Median spatial filtering enhances these features when there are multiple nearby stations. In Figure 6a we see that GPS Imaging isolates these signals from the surrounding vertical velocity field for Mt. Lassen, Medicine Lake in Northern California, and the Long Valley Caldera system (locations in Figure 1). All of these volcanoes are active; Mt. Lassen had significant eruptive activity starting in 1914 and continuing for several years [Clynne *et al.*, 1999], the most recent flow at Medicine Lake occurred ~950 years ago [Donnelly-Nolan *et al.*, 2007], and Long Valley has experienced several episodes of unrest over the past several decades [Hill, 2006]. The signals vary in sign, Long Valley trends upward, and Mt. Lassen and Medicine Lake are subsiding, suggesting that they are in different parts of their volcanic cycles.

#### 5.1.1. Medicine Lake

Of the three, deformation at Medicine Lake is least well constrained, with only three GPS stations, although all are subsiding. Each of these stations collected data from late 2005/early 2006 to the present. MIDAS velocities and uncertainties for these stations are  $-0.86 \pm 0.72$  for P672,  $-4.51 \pm 1.16$  mm/yr for P673, and  $-1.83 \pm 0.79$  mm/yr for P674. P672 is the furthest (13 km) from the subsidence center, while the other two (P673 is 4 km and P674 is 6 km) subside more rapidly. These stations are far enough from

distinct periods of uplift pre-2010 and post-2010. Patterns over this period are similar in geographic distribution, but the uplift along the length of the Sierra Nevada Range is faster post-2011. Pre-2011 Sierra Nevada uplift velocity is 0.5 to 1.0 mm/yr, and the late period velocities are approximately twice as fast. An implication of this observation is that a background tectonic uplift may be present at all times at the lower, pre-2011 rate. Some net water mass loss or gain may have occurred in the pre-2011 period so the rate of tectonic uplift is still uncertain.

Owing to the finite volume of the water available in the Central Valley aquifers, it is not likely that drought-related mass loss will continue indefinitely into the future. If in the

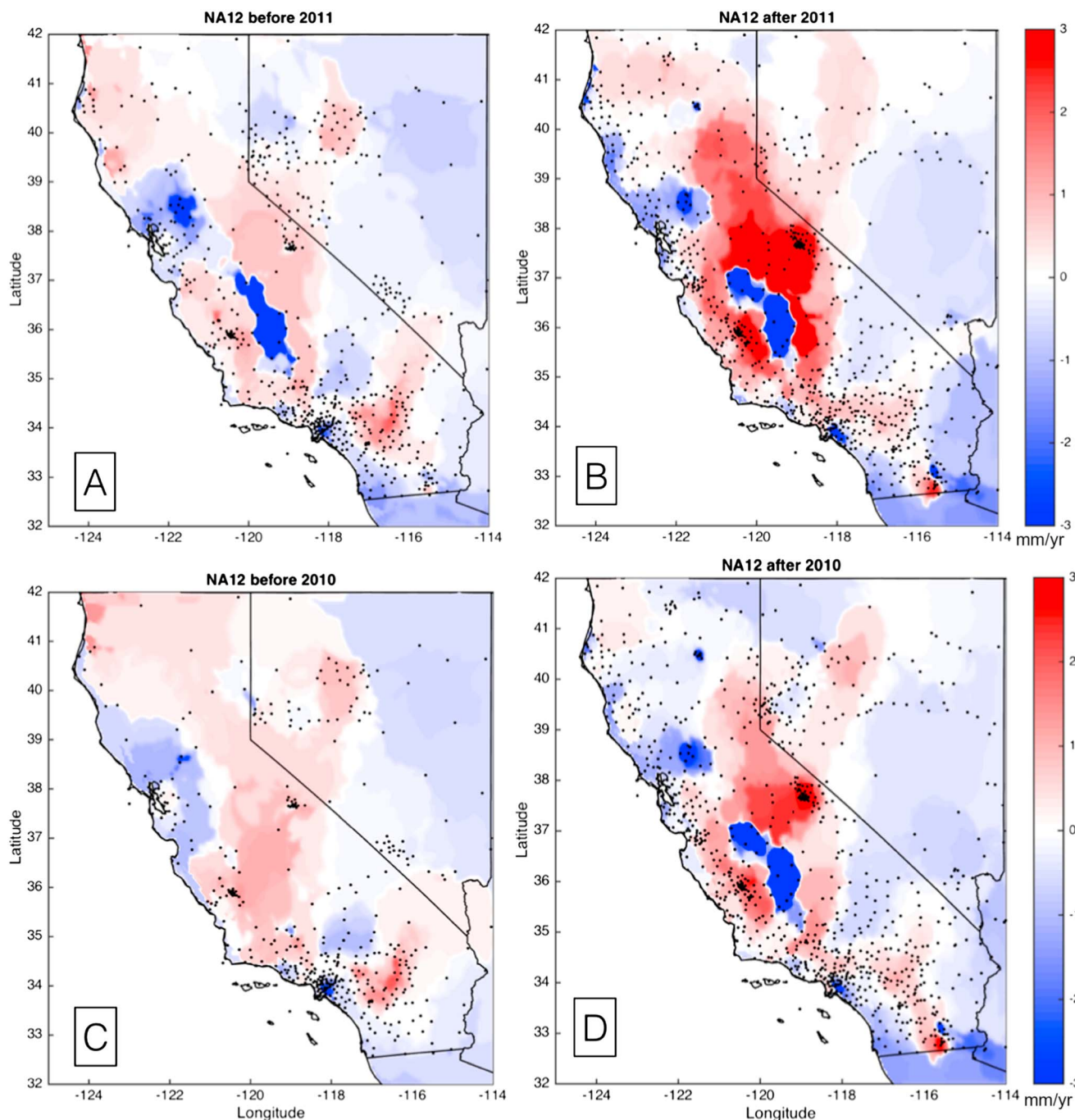


**Figure 11.** (a) Image of vertical rate from time series of minimum duration 5 years before year 2011.0, (b) after 2011.0, (c) before 2010.0, and (d) after 2010.0. The dots are the locations of GPS stations contributing to the image. The color scale is the same as in previous figures.

the subsidence center that they do not sample the fastest velocities on the order of  $-10\text{ mm/yr}$  that have been observed with interferometric synthetic aperture radar (InSAR), campaign GPS, and leveling [Dzurisin et al., 1991, 2002; Poland et al., 2006; Parker et al., 2014]. The image has subsidence rates of  $-2\text{ mm/yr}$  within an area centered on the magmatic system and thus underrepresents the maximum velocity owing to the lack of GPS data at source center. However, despite the sparseness of GPS observation, and because the volcanic center is surrounded by other more stable stations at various distances and various azimuths, our technique images a focused spot of subsidence that is consistent with an isolated magmatic source.

### 5.1.2. Lassen Peak

At Lassen Peak all stations within 11 km of the summit, in all azimuths around the edifice, subside, suggesting a large and/or deep source. The median velocity of those stations is  $-6.1$  mm/yr, constrained by MIDAS velocities from eight GPS stations. MIDAS appears to be estimating the trends well in spite of vertical position excursions on at least six of these stations in winter seasons, attributable to snow shielding the antennas. Subsidence is generally faster near the edifice. These results are roughly consistent with those of *Poland et al.* [2004] and *Parker et al.* [2016], who used InSAR to detect  $\sim 10$  mm/yr subsidence in 30–40 km diameter area centered 5 km southeast of the Lassen Peak. *Parker et al.* [2015] noted that a significant portion of the signal in Envisat data from 2004 to 2010 was attributable to topographically correlated atmospheric noise in the interferograms. Atmospheric effects are estimated and removed in our GPS positioning, confirming that significant ground deformation also contributes to these signals.

### 5.1.3. Long Valley Caldera

Unrest and magmatic intrusion at the Long Valley Caldera are monitored continuously, and uplift has been attributed to episodic volumetric changes of an inclined ellipsoidal magmatic body near 6–14 km depth [*Fialko et al.*, 2001; *Langbein*, 2003; *Hill*, 2006; *Feng and Newman*, 2009; *Montgomery-Brown et al.*, 2015]. The median MIDAS uplift velocity for stations in the caldera is 3.9 mm/yr, and the image has a median velocity of 2.9 mm/yr upward, although this is a general trend through a highly time variable inflation. It is not clear from Figure 6a where the boundary between Sierra Nevada Range uplift and Long Valley magmatic uplift lies. Deformation models of the inflation could be used to estimate and remove the nonsteady magmatic contribution, correcting the time series prior to imaging. That is beyond the scope of this paper but could potentially better reveal the location of the eastern limit of Sierra Nevada range uplift and whether it intersects the Long Valley Caldera.

## 5.2. Central Valley Subsidence

The strongest signal in Figure 6 is by far subsidence in the Central Valley of California, which is fully saturated on the negative end of the color scale. Subsidence is present throughout most of the San Joaquin Valley at rates far exceeding the uplift in the surrounding Coast Ranges and Sierra Nevada (this uplift is discussed in detail in section 5.4). While consistently downward, the image shows that Central Valley subsidence is discontinuous and divided into three major subsidence zones, coincident with the InSAR-imaged basins centered at El Nido and Corcoran [*Farr et al.*, 2015] and the southwestern Sacramento Valley [*Bürgmann*, 2008]. The perimeters of the subsiding regions are also roughly coincident with the areas of historical subsidence in the Central Valley and consistent with its source being compaction of materials within the aquifers related to groundwater extraction [*Faunt et al.*, 2009]. While the number of GPS stations has increased greatly over time (Figure 10) there are still limits on the resolution of the shape of subsidence area perimeters, owing to incomplete and variable density of coverage. The exact perimeters separating the subsiding and uplifting areas in the Central Valley is sensitive to station sampling.

## 5.3. Earthquake Cycle and Tectonic Deformation

### 5.3.1. Cascadia Subduction Zone and Mendocino Triple Junction

In the northwest corner of Figure 6a, adjacent to the Pacific coast, we see the effects of Cascadia interseismic strain accumulation from locking of the subducting Gorda slab with North America. The velocities in the image are consistently upward except along the west coast near Cape Mendocino, e.g., P159, P161, and P162 and the cluster at CME1, CME2, CME5, and CME6. From integrated analysis of leveling and tide gauges, *Burgette et al.* [2009] found uplift rates between 2 and 4 mm/yr near Crescent City, California. This range of vertical velocities is consistent with the MIDAS velocity for the GPS station at Point St. George  $3.3 \pm 0.7$  mm/yr, and the maximum uplift rate in the image, 2.3 mm/yr near latitude  $42^\circ$ .

We also find a zone of uplift that penetrates inland nearly to the longitude of the Sacramento Valley ( $-122.4^\circ$  longitude; Figures 1 and 6), although this signal is near the level of the uncertainties, which are  $\sim 0.5$  mm/yr in this area (Figure 7). Uplift here could be related to crustal contraction since it is confined between the subducting Gorda slab, northwest migrating Sierra Nevada/Central Valley microplate into the Klamath Mountains [*Hemphill-Haley*, 1999; *Williams et al.*, 2006], and slower northward translation of the Oregon Coast fore-arc microplate to the north [*Wells and Simpson*, 2001; *McCaffrey et al.*, 2013]. Whether the Klamath uplift can be best interpreted as a plastic flow or recoverable strain on faults is uncertain. Nearer the coast vertical rates may be associated with the recent passage of the Mendocino Triple Junction (MTJ),

which initiated a wave of ephemeral uplift estimated to occur at  $\sim 0.9$  mm/yr followed by subsidence at  $\sim -0.8$  mm/yr [Furlong and Govers, 1999]. The predictions of that model are consistent with the change in GPS vertical velocity sign from positive north of to negative south of  $\sim 39.7^\circ$  latitude south of Cape Mendocino. This process could be related to the observed Coast Range subsidence between the MTJ and the San Francisco Bay Area.

### 5.3.2. Postseismic Deformation

The images in Figure 6 show an uplift feature that is centered over the Central Nevada Seismic Belt (CNSB), a zone where most of the twentieth century seismic moment in Nevada has been released. The uplift pattern and rates are consistent with previous imaging based on InSAR [Gourmelen and Amelung, 2005] and earlier images based on GPS [Hammond et al., 2012]. We now have a greater number of stations with over 5 year time series duration that bound the anomaly on the east, west, and south. MAGNET network stations to the north of the anomaly have been established and surveyed multiple times but have not yet reached our cutoff threshold of 5 year time series duration and thus do not contribute to the results shown in Figure 6a. GPS time series with shorter duration are less reliable for vertical velocity studies, but we nonetheless test to see if more detail can be obtained in the image using time series with a minimum of 2.5 year duration (Figure 6c). This image shows that the CNSB postseismic relaxation bulge may continue northward as far as  $41.2^\circ$  latitude, possibly dissipating north of there. This is consistent with the northernmost end of CNSB surface rupture extending to nearly  $41.0^\circ$  latitude (Figure 1). The maximum upward individual GPS velocity is  $1.8 \pm 0.76$  mm/yr, while the image has a maximum value of 1.0 mm/yr. While many of the individual MIDAS GPS velocities are not significantly different than zero at 95% confidence (Figure 12), the image has lower uncertainty because of the combined power of multiple stations contributing to every image pixel.

The uplift pattern is consistent with predictions from models of viscoelastic postseismic relaxation following the CNSB events and is consistent with an anomaly in horizontal strain rates expected from models [Hetland and Hager, 2003; Hammond and Thatcher, 2004; Pollitz et al., 2008; Hammond et al., 2009]. While estimates of the viscosities of the lower crust and upper mantle differ somewhat among the various studies [Thatcher and Pollitz, 2008], the interpretation of the uplift anomaly as a long-lived viscoelastic response seems to be agreed upon. More detailed modeling with realistic rheological properties that integrates coseismic, early, and later postseismic deformation suggests that a symmetric uplift response in the later postseismic period is expected, that the deformation source is mantle flow immediately beneath the crust, and that the mechanical lithosphere is  $\sim 40$  km deep [Thompson and Parsons, 2016; Dickenson et al., 2016].

We also see uplift in the southern Mojave in the vicinity of the 1992 Landers and 1999 Hector Mine strike-slip earthquakes. This uplift is markedly different than the pattern seen in the postseismic period immediately (days to a few years) following the individual Landers and Hector Mine events that had quadlobate fields with alternating positively and negatively signed uplifts [Pollitz et al., 2001; Freed et al., 2007; Takeuchi and Fialko, 2013].

### 5.3.3. San Andreas Fault System

The uplift we observe along the San Andreas Fault (SAF) system has similarities to the modeling results of Smith-Konter et al. [2014]. Their semianalytic model of the vertical velocity field is based on relative plate motion across the fault, the history of earthquakes, variations in locking depth, creep state, and postseismic response in a realistic rheological structure. However, the subsidence in California Central Valley suggests that the SAF earthquake cycle along the central California section is partly obscured by the signal of decadal trends in groundwater unloading [Amos et al., 2014]. The southern section of the SAF, however, should not be strongly effected and shows a stripe of uplift from the Salton Trough northward, through the San Bernardino and Mojave sections of the SAF, and through the Big Bend into central California (Figures 3 and 6). The observed anomaly does not appear to be quite as intense or as narrowly focused as the prediction of Smith-Konter et al. [2014] but does align with the overall feature. Their modeling also shows velocities generally below zero north of the San Francisco Bay Area, offering an alternative to the mechanisms we discuss in section 5.3.1.

## 5.4. Sierra Nevada Uplift

Uplift of the Sierra Nevada occurs along nearly the entire length of the range, from the Garlock fault in the south to the latitude of Lake Tahoe ( $39^\circ\text{N}$ ) in the north. Uplift rates are between 1 and 2 mm/yr, except at the volcanic systems discussed above. In particular, the uplift is somewhat faster in areas adjacent to the

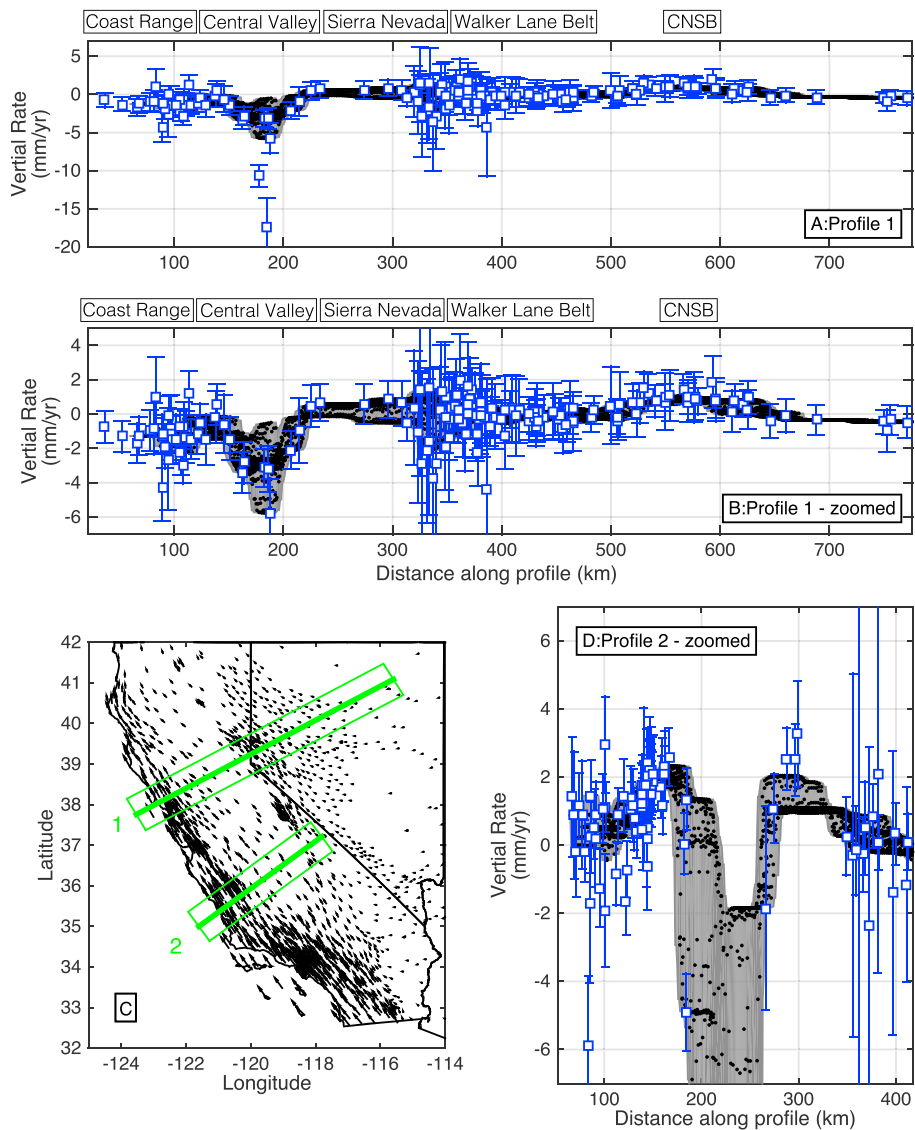


**Figure 12.** Profiles of vertical GPS velocity across California and Nevada as function of distance along profiles. (a) Profile 1 with location of key tectonic provinces shown with annotation. (b) Profile 1 with vertical axis zoomed in to better reveal details of data, uncertainties, and GPS Imaging model. The vertical bars are the 2 sigma uncertainties. The gray region is the envelope of the GPS Imaging result (black dots); width of which is attributable to cross-profile variation in the imaged rate. (c) Number and location of profiles shown over horizontal GPS velocities. (d) The zoomed version of profile 2 with vertical axis exaggeration to show relation between image and data.

fastest subsidence in the Central Valley (Figure 6). This is further evidence of a causal relationship between Central Valley subsidence and Sierra/Coast Range uplift and that this uplift is in part a response to climate change and anthropogenic groundwater extraction resulting in unburdening of the lithosphere [Amos *et al.*, 2014].

However, the correlation between valley subsidence and flank uplift is not perfect. While the Sierra Nevada uplift is contiguous from 34.5° to 39.2° latitude, Central Valley subsidence is discontinuous as noted in section 5.2. Furthermore, in the northern half of the Sacramento Valley, we do not see the uplift to the west of the subsidence as we do to the south, where the uplift around the San Joaquin Valley is east-west symmetric. This may be because the Sacramento Valley subsidence is less intense than that in the SJV. Figure 12 shows the vertical velocity profiles that cross the axis of the Central Valley at the latitudes of the Sacramento and San Joaquin Valleys. They show that subsidence rates in the Sacramento Valley are about

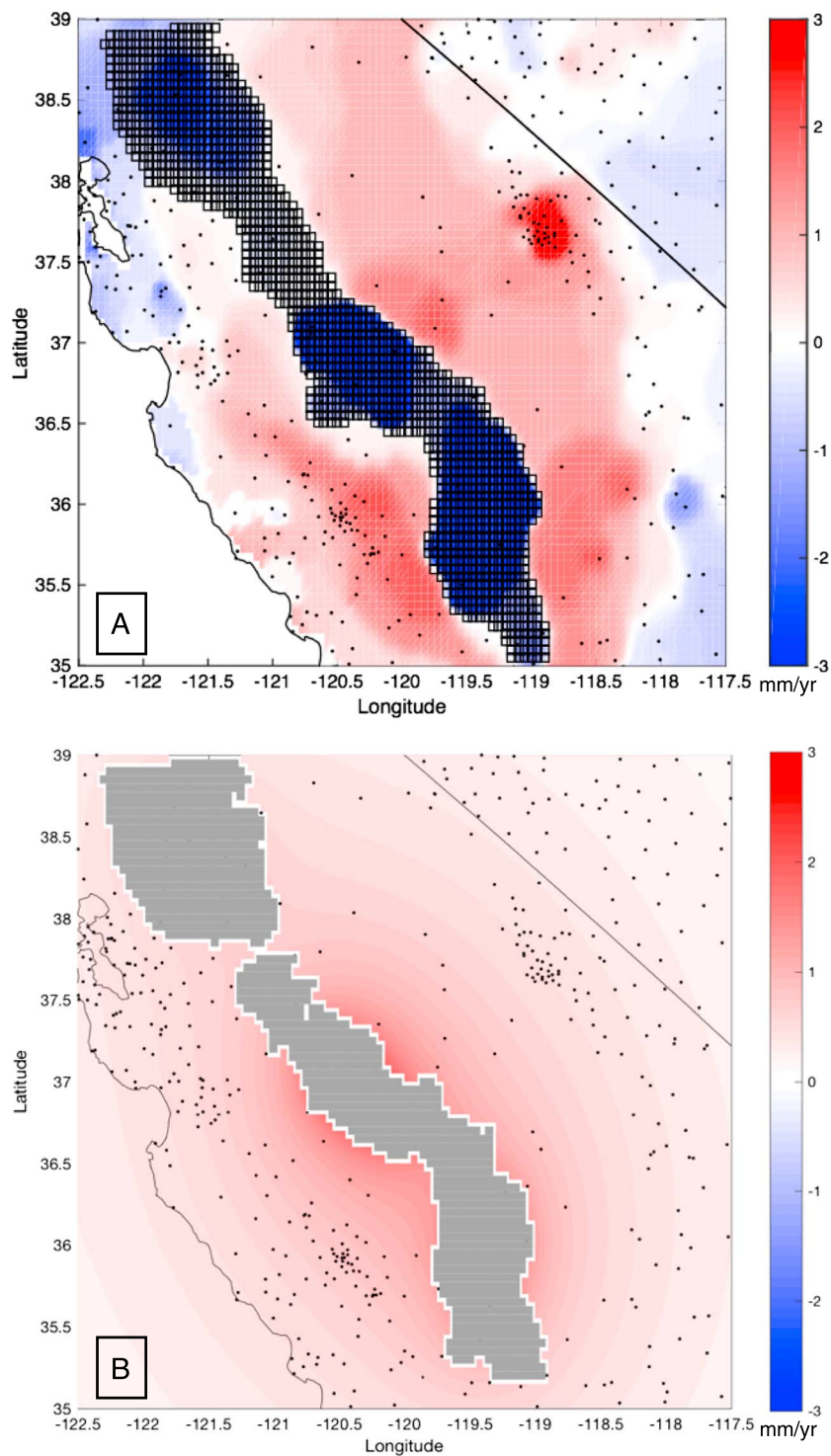


**Figure 13.** (a) Hypothetical load of lost water mass implied by distribution of subsidence in Great Valley of California (tiled black squares), superimposed on segment of map shown in Figure 6a. (b) Modeled vertical displacement response to load change assuming elastic half-space, where maximum response outside of loading area is scaled to 2 mm/yr. The color scale is in mm/yr.

–6 mm/yr but locally faster at some stations, while in the San Joaquin Valley the image is subsiding near –60 mm/yr. Thus, slower uplift on the flanks of the Sacramento Valley is expected, and possibly, other processes such as those discussed in sections 5.3.1 and 5.3.3 above could mask part or all of it on the west of the valley.

The difference in patterns between subsidence and uplift suggests that not all Sierra Nevada uplift is driven by groundwater withdrawal; i.e., a background tectonic uplift may contribute to the signal. Further evidence comes from the sharp discontinuity between upward and downward velocities in the image that coincides almost perfectly with the eastern boundary of the Sierra Nevada/Central Valley microplate, bounding the Sierra Nevada and western Basin and Range (Figure 6a). The checkerboard test shows that this feature is not an artifact of the GPS network distribution. The transition was previously observed the GPS data [Fay *et al.*, 2008]. Here we show its continuity as far north as Lake Tahoe.

The signal of uplift driven by unloading from groundwater extraction in the Central Valley is expected to decrease asymptotically with distance from the valley and is not expected be discontinuous. We illustrate this by modeling the hydrological mass using an array of rectangular loads on an elastic half-space [Becker and Bevis, 2004]. At  $0.05^\circ \times 0.05^\circ$  patches that are distributed over areas in the Central Valley where the image shows downward motion, we apply a negative load proportional to the downward velocity in the GPS image at the location of the patch. We sum the responses and then scale the sum so that the maximum uplift response matches the maximum Sierra Nevada uplift in the image (Figure 13a). We can see from the modeled response (Figure 13b) that there is no expected truncation of the response at the eastern edge of the Sierra Nevada, such as is observed in the GPS image. Nor is the response as discontinuous as the input subsidence pattern, since the elastic half-space smoothes the response to the load. This suggests that the observed response is attributable to loads different from the major subsidence zones in the Central Valley, e.g., tectonic forces, or that the assumptions of this simple model have been violated; e.g., the medium is not an elastic half-space.

It is likely that the Sierra Nevada range front near the southern Walker Lane/Owens Valley is free to uplift more rapidly owing to a lithospheric-scale strength transition, a possibility discussed in context of GPS observations by Bennett *et al.* [2009]. It may be that the Owens Valley lithosphere has been damaged by repeated earthquakes that have amassed many kilometers of cumulative displacement [Wesnousky, 2005] and is weakened by other past tectonic events in an extensional arc that became an active and complex transtensional shear zone [Oldow *et al.*, 2008; Busby, 2013]. In either case, geodynamic studies agree that the Walker Lane lithosphere is weak compared to the SNCV microplate [Flesch *et al.*, 2000; Malservisi *et al.*, 2001; Fay and Humphreys, 2008], a point supported by the relative rigidity of the SNCV compared to the Walker Lane [Argus and Gordon, 1991; Dixon *et al.*, 2000]. The present location of this weakness may be a snapshot in the westward migration of the western limit of SWL shear and uplift over the last 5 Myr [Jones *et al.*, 2004], a migration that may still be on its way into the SNCV in the southern Sierra today [Unruh *et al.*, 2014]. Such a lithospheric strength contrast may focus tectonic uplift in the southern Sierra, irrespective of the source of forces that drive it, and possibly helps the SNCV respond vertically as a coherent block, i.e., providing a geographically coherent uplift from Central Valley to Sierra Crest rather than bending near a locked eastern edge. This strength contrast may persist northward along the length of the Sierra Nevada/Great Basin transition, where Moho depth seismicity swarms near Lake Tahoe and Sierraville (Figure 1) reveal lower crustal diking that suggest active rifting along this boundary [Smith *et al.*, 2016]. This broken plate model could also help to explain the observations with only groundwater unloading, since disengaging the SNCV from areas further east could allow the rebound to be truncated at the Owens Valley. In either case, the strength contrast helps explain the observations and show how new geodetic data can provide a lens through which to view contrasts in lithospheric strength.

## 6. Conclusions

We have described a new method, GPS Imaging, for selecting, filtering, and interpolating vertical velocities in order to generate robust maps of the vertical velocity field associated with flex and flow of the solid Earth. The technique can best be described as a hybrid between image-processing-style median spatial filtering and geostatistical kriging. Signals that are present at multiple stations are preserved, and the velocity field is despeckled resulting in enhanced interpretive value of GPS data. The technique utilizes both the temporal robustness of MIDAS trend estimator [Blewitt *et al.*, 2016] and spatial robustness of the weighted median spatial filtering. Together these methods allow recognition of the signals of elastic strain accumulation on faults, magmatic deformation, viscous postseismic relaxation, tectonic uplift, subsidence from groundwater extraction, and related elastic rebound. Signals from all of these processes contribute to the vertical velocity field in California and Nevada.

GPS Imaging shows that the Sierra Nevada experiences active uplift along nearly the entire length of the range, from the Garlock Fault to the latitude of Lake Tahoe. The uplift is stable over two completely independent segments of time in the data, though rises faster over the post-2011.0 period of drought in California. The spatial and temporal patterns of uplift suggest that signals of both groundwater extraction in the Central Valley of California and background tectonic uplift may be present and delineate an important lithospheric strength contrast along the Sierra Nevada/Basin and Range transition.

### Acknowledgments

The original data used in this analysis were obtained from GPS networks in California and Nevada, whose data are available in the public domain. We thank UNAVCO for collecting and archiving the GPS data in the EarthScope Plate Boundary Observatory and its nucleus networks; the USGS and UC Berkeley for operating the BARD network; the USGS, Scripps, and JPL for operating the SCIGN; the NGS for supporting the CORS cooperative network; Central Washington University for operating the PANGA; the IGS for operating the IGS core network; and Las Vegas Valley Water District, Arizona Height Modernization Program, AZGPS, California Surveying and Drafting Supply, and Washoe county for sharing the data from their networks. Specific server internet addresses for data are provided in Table S1. We thank the Jet Propulsion Laboratory for the use of the GIPSY software and for the data products used in the GPS data processing. Direct research support for this project came from the NSF EarthScope program for the project “Revealing the Nature of Contemporary Uplift and Collapse in the Sierra Nevada-Great Basin System” (0844389 and 1252210) to G.B. and W.C. H. We thank NASA for the support of GPS data processing through the ROSES Sea Level Rise (NNX14AJ98G) and ACCESS programs (NNX14AJ52A). Surveying of the MAGNET GPS network was supported by the USGS NEHRP grants G10AC00138 and G15AC00078 and NSF-EAR projects 0610031, 0635757, and 0952166. We thank Janet Becker for sharing the Love’s problem software. Figure 1 was drawn with the Generic Mapping Tools software [Wessel and Smith, 1998]. We thank Jeff Freymueller, an anonymous reviewer, and Associate Editor Mike Poland for their comments that substantially improved this manuscript.

### References

- Altamimi, Z., X. Collilieux, and L. Métivier (2011), ITRF2008: An improved solution of the International Terrestrial Reference Frame, *J. Geod.*, **85**, 457–473, doi:10.1007/s00190-011-0444-4.
- Amos, C. B., P. Audet, W. C. Hammond, R. Bürgmann, I. A. Johanson, and G. Blewitt (2014), Uplift and seismicity driven by groundwater depletion in central California, *Nature*, doi:10.1038/nature13275.
- Aoki, Y., and C. H. Scholz (2003), Vertical deformation of the Japanese islands, 1996–1999, *J. Geophys. Res.*, **108**(B5), 2257, doi:10.1029/2002JB002129.
- Argus, D. F., and R. G. Gordon (1991), Current Sierra Nevada-North America motion from very long baseline interferometry: Implications for the kinematics of the western United States, *Geology*, **19**, 1085–1088.
- Argus, D. F., Y. Fu, and F. W. Landerer (2014), Seasonal variation in total water storage in California inferred from GPS observations of vertical land motion, *Geophys. Res. Lett.*, **41**, 1971–1980, doi:10.1002/2014GL059570.
- Barbot, S., Y. Fialko, and Y. Bock (2009), Postseismic deformation due to the  $M_w$  6.0 2004 Parkfield earthquake: Stress-driven creep on a fault with spatially variable rate-and-state friction parameters, *J. Geophys. Res.*, **114**, B07405, doi:10.1029/2008JB005748.
- Beavan, J., P. Denys, M. Denham, B. Hager, T. Herring, and P. Molnar (2010), Distribution of present-day vertical deformation across the Southern Alps, New Zealand, from 10 years of GPS data, *Geophys. Res. Lett.*, **37**, L16305, doi:10.1029/2010GL044165.
- Becker, J., and M. Bevis (2004), Love’s problem, *Geophys. J. Int.*, **156**, 171–178, doi:10.1111/j.1365-246X.2003.02150.x.
- Bennett, R. A., N. P. Fay, S. Hreinsdóttir, C. Chase, and G. Zandt (2009), Increasing long-wavelength relief across the southeastern flank of the Sierra Nevada, California, *Earth Planet. Sci. Lett.*, **287**, 255–264, doi:10.1016/j.epsl.2009.08.011.
- Berke, O. (2001), Modified median polish kriging and its application to the Wolfcamp-Aquifer data, *Environmetrics*, **12**, 731–748, doi:10.1002/env.495.
- Bertiger, W., S. D. Desai, B. Haines, N. Harvey, A. W. Moore, S. Owen, and J. P. Weiss (2010), Single receiver phase ambiguity resolution with GPS data, *J. Geod.*, **84**(5), 327–337, doi:10.1007/s00190-010-0371-9.
- Blewitt, G., Hammond, W. C., Kreemer, C. (2009), Geodetic constraints on contemporary deformation in the Northern Walker Lane: 1, Semi-permanent GPS strategy, in *Late Cenozoic Structure and Evolution of the Great Basin-Sierra Nevada Transition*, edited by J. S. Oldow, and P. H. Cashman, *Geol. Soc. Am. Spec. Pap.*, **447**, 1–16, doi:10.1130/2009.2447(01).
- Blewitt, G., C. Kreemer, W. C. Hammond, and J. Goldfarb (2013), Terrestrial reference frame NA12 for crustal deformation studies in North America, *J. Geodyn.*, **72**, 11–24, doi:10.1016/j.jog.2013.08.004.
- Blewitt, G., C. Kreemer, W. C. Hammond, and J. Gazeaux (2016), MIDAS robust trend estimator for accurate GPS station velocities without step detection, *J. Geophys. Res. Solid Earth*, **121**, 2054–2068, doi:10.1002/2015JB012552.
- Borsa, A. A., D. C. Agnew, and D. R. Cayan (2014), Ongoing drought-induced uplift in the western United States, *Science*, **345**(6204), 1587–1590.
- Burgette, R. J., R. J. Weldon II, and D. A. Schmidt (2009), Interseismic uplift rates for western Oregon and along-strike variation in locking on the Cascadia subduction zone, *J. Geophys. Res.*, **114**, B01408, doi:10.1029/2008JB005679.
- Bürgmann, R. (2008), Deformation and earthquake potential of the eastern Coast Ranges from PS-InSAR measurements, USGS NEHRP Final Tech. Rep., Project: 08-HQGR-0095.
- Bürgmann, R., and G. Dresen (2008), Rheology of the lower crust and upper mantle: Evidence from rock mechanics, geodesy, and field observations, *Annu. Rev. Earth Planet. Sci.*, **36**, 531–67, doi:10.1146/annurev.earth.36.031207.124326.
- Bürgmann, R., G. Hilley, A. Ferretti, and F. Novali (2006), Resolving vertical tectonics in the San Francisco Bay Area from permanent scatterer InSAR and GPS analysis, *Geology*, **34**(3), 221–224, doi:10.1130/G22064.1.
- Busby, C. (2013), Birth of a plate boundary at ca. 12 Ma in the Ancestral Cascades arc, Walker Lane belt of California and Nevada, *Geosphere*, **9**(5), 1147–1160, doi:10.1130/GES00928.1.
- Castleman, K. R. (1996), *Digital Image Processing*, pp. 667, Prentice Hall, Upper Saddle River, N. J.
- Ching, K.-E., R.-J. Rau, K. M. Johnson, J.-C. Lee, and J.-C. Hu (2011), Present-day kinematics of active mountain building in Taiwan from GPS observations during 1995–2005, *J. Geophys. Res.*, **116**, B09405, doi:10.1029/2010JB008058.
- Clynne, M. A., R. L. Christiansen, T. J. Felger, P. H. Stauffer, and J. W. Hendley (1999), Eruptions of Lassen Peak, California, 1914 to 1917, *U.S. Geol. Surv. Fact Sheet*, **172**–98, 2. [Available at <http://pubs.usgs.gov/fs/1998/fs173-98/>.]
- Conrad, C. P. (2013), The solid Earth’s influence on sea level, *GSA Bull.*, **125**(7/8), 1027–1052, doi:10.1130/B30764.1.
- Cormen, T. H., C. E. Leiserson, R. L. Rivest, and C. Stein (2001), *Introduction to Algorithms*, MIT Press, Cambridge, Mass., isbn:9780262032933.
- Cressie, N. (1990), The origins of kriging, *Math. Geol.*, **22**(3), 239–252.
- Delaunay, B. (1934), Sur la sphère vide, *Bull. Acad. Sci. USSR*, **7**, 793–800.
- Dickinson, H., A. M. Freed, and C. Andronicos (2016), Inference of the viscosity structure and mantle conditions beneath the Central Nevada Seismic Belt from combined postseismic and lake unloading studies, *Geochem. Geophys. Geosyst.*, **17**, 1740–1757, doi:10.1002/2015GC006207.
- Dixon, T. H., M. Miller, F. Farina, H. Wang, and D. Johnson (2000), Present-day motion of the Sierra Nevada block and some tectonic implications for the Basin and Range Province, North American Cordillera, *Tectonics*, **19**(1), 1–24, doi:10.1029/1998TC001088.
- Donnelly-Nolan, J. M., M. Nathenson, D. E. Champion, D. W. Ramsey, J. B. Lowenstern, and J. W. Ewert (2007), Volcano hazards assessment for Medicine Lake Volcano, Northern California, *U.S. Geol. Surv. Sci. Invest. Rep.*, **2007-5174-A**, 26.
- Dzurisin, D., J. M. Donnelly-Nolan, J. R. Evans, and S. R. Walter (1991), Crustal subsidence, seismicity, and structure near Medicine Lake volcano, California, *J. Geophys. Res.*, **96**(B10), 16,319–16,333, doi:10.1029/91JB01452.
- Dzurisin, D., M. P. Poland, R. Bürgmann (2002), Steady subsidence of Medicine Lake volcano, Northern California, revealed by repeated leveling surveys, *J. Geophys. Res.*, **107**(B12), 2372, doi:10.1029/2001JB000893.
- Farr, T. G., C. Jones, and Z. Liu (2015), Progress Report: Subsidence in the Central Valley, California, NASA report prepared for California Department of Water Resources. [Available at [http://water.ca.gov/groundwater/docs/NASA\\_REPORT.pdf](http://water.ca.gov/groundwater/docs/NASA_REPORT.pdf).]

- Faunt, C. C., K. Belitz, and R. T. Hanson (2009), Groundwater availability in California's Central Valley, in *Groundwater Availability of the Central Valley Aquifer, California, U.S. Geol. Surv. Prof. Pap.*, 1766, 225.
- Fay, N. P., and E. D. Humphreys (2008), Forces acting on the Sierra Nevada block and implications for the strength of the San Andreas fault system and the dynamics of continental deformation in the western United States, *J. Geophys. Res.*, 113, B12415, doi:10.1029/2008JB005809.
- Fay, N. P., R. A. Bennett, and S. Hreinsdóttir (2008), Contemporary vertical velocity of the central Basin and Range and uplift of the southern Sierra Nevada, *Geophys. Res. Lett.*, 35, L20309, doi:10.1029/2008GL034949.
- Feng, L., and A. V. Newman (2009), Constraints on continued episodic inflation at Long Valley Caldera, based on seismic and geodetic observations, *J. Geophys. Res.*, 114, B06403, doi:10.1029/2008JB006240.
- Fialko, Y. (2004), Evidence of fluid-filled upper crust from observations of postseismic deformation due to the 1992  $M_w$ 7.3 Landers earthquake, *J. Geophys. Res.*, 109, B08401, doi:10.1029/2004JB002985.
- Fialko, Y., M. Simons, and Y. Khazan (2001), Finite source modelling of magmatic unrest in Socorro, New Mexico, and Long Valley, California, *Geophys. J. Int.*, 146, 191–200.
- Flesch, L. M., W. E. Holt, A. J. Haines, and B. Shen-Tu (2000), Dynamics of the Pacific–North American Plate boundary in the western United States, *Science*, 287, 834–836.
- Freed, A. M., R. Bürgmann, and T. Herring (2007), Far-reaching transient motions after Mojave earthquakes require broad mantle flow beneath a strong crust, *Geophys. Res. Lett.*, 34, L19302, doi:10.1029/2007GL030959.
- Fu, Y., and J. T. Freymueller (2012), Seasonal and long-term vertical deformation in the Nepal Himalaya constrained by GPS and GRACE measurements, *J. Geophys. Res.*, 117, B03407, doi:10.1029/2011JB008925.
- Fu, Y., D. F. Argus, and F. W. Landerer (2014), GPS as an independent measurement to estimate terrestrial water storage variations in Washington and Oregon, *J. Geophys. Res. Solid Earth*, 120, 552–566, doi:10.1002/2014JB011415.
- Furlong, K. P., and R. Govers (1999), Ephemeral crustal thickening at a triple junction: The Mendocino crustal conveyor, *Geology*, 27(2), 127–130.
- Gourmelen, N., and F. Amelung (2005), Postseismic mantle relaxation in the Central Nevada Seismic Belt, *Science*, 310, 1473–1476.
- Haines, A. J., and W. E. Holt (1993), A procedure for obtaining the complete horizontal motions within zones of distributed deformation from the inversion of strain rate data, *J. Geophys. Res.*, 98(B7), 12,057–12,082, doi:10.1029/93JB00892.
- Hamlington, B. D., P. Thompson, W. C. Hammond, G. Blewitt, and R. D. Ray (2016), Assessing the impact of vertical land motion on 20th century global mean sea level estimates, *J. Geophys. Res. Oceans*, 121, 4980–4993, doi:10.1002/2016JC011747.
- Hammond, W. C., and W. Thatcher (2004), Contemporary tectonic deformation of the Basin and Range Province, western United States: 10 years of observation with the Global Positioning System, *J. Geophys. Res.*, 109, B08403, doi:10.1029/2003JB002746.
- Hammond, W. C., Kreemer, C., Blewitt, G. (2009), Geodetic constraints on contemporary deformation in the Northern Walker Lane: 3, Central Nevada seismic belt postseismic relaxation, in *Late Cenozoic Structure and Evolution of the Great Basin–Sierra Nevada Transition*, edited by J. S. Oldow, and P. H. Cashman, *Geol. Soc. Am. Spec. Pap.*, 447, 33–54, doi:10.1130/2009.2447(03).
- Hammond, W. C., G. Blewitt, Z. Li, C. Kreemer, and H.-P. Plag (2012), Contemporary uplift of the Sierra Nevada, western United States, from GPS and InSAR measurements, *Geology*, 40, 667–670, doi:10.1130/G32968.1.
- Hemphill-Haley, M. A. (1999), Multi-scaled analyses of contemporary crustal deformation of western North America, PhD thesis, 237 pp., Univ. of Oreg., Eugene.
- Hetland, E. A., and B. H. Hager (2003), Postseismic relaxation across the Central Nevada seismic belt, *J. Geophys. Res.*, 108(B8), 2394, doi:10.1029/2002JB002257.
- Hill, D. (2006), Unrest in Long Valley Caldera, California, 1978–2004, in *Mechanisms of Activity and Unrest at Large Calderas*, edited by C. Troise, G. De Natale, and C. R. J. Kilburn, *Geol. Soc. London, Spec. Publ.*, 269, 1–24.
- Holzer, T. L. (1979), Elastic expansion of the lithosphere caused by groundwater depletion, *J. Geophys. Res.*, 84, 4689–4698, doi:10.1029/JB084iB09p04689.
- Jones, C. H., G. L. Farmer, and J. Unruh (2004), Tectonics of Pliocene removal of lithosphere of the Sierra Nevada, California, *GSA Bull.*, 116(11/12), 1408–1422, doi:10.1130/B25397.1.
- Kreemer, C., G. Blewitt, and E. C. Klein (2014), A geodetic plate motion and global strain rate model, *Geochem. Geophys. Geosyst.*, 15, 3849–3889, doi:10.1002/2014GC005407.
- Krige, D. G. (1951), A statistical approach to some mine valuations and allied problems at the Witwatersrand, Master's thesis, Univ. of Witwatersrand, Johannesburg, South Africa.
- Langbein, J. O. (2003), Deformation of the Long Valley Caldera, California: Inferences from measurements from 1988 to 2001, *J. Volc. Geothermal Res.*, 127, 247–267, doi:10.1016/S0377-0273(03)00172-0.
- Liu, Z., D. Dong, and P. Lundgren (2011), Constraints on time-dependent volcanic source models at Long Valley Caldera from 1996 to 2009 using InSAR and geodetic measurements, *Geophys. J. Int.*, 187, 1283–1300, doi:10.1111/j.1365-246X.2011.05214.x.
- Malservisi, R., K. P. Furlong, and T. H. Dixon (2001), Influence of the earthquake cycle and lithospheric rheology on the dynamics of the Eastern California Shear Zone, *Geophys. Res. Lett.*, 28(14), 2731–2734, doi:10.1029/2001GL013311.
- Marshall, S. T., G. J. Funning, and S. E. Owen (2013), Fault slip rates and interseismic deformation in the western Transverse Ranges, California, *J. Geophys. Res. Solid Earth*, 118, 4511–4534, doi:10.1002/jgrb.50312.
- Matheron, G. (1963), Principles of geostatistics, *Econ. Geol.*, 58(8), 1246–1266, doi:10.2113/gsecongeo.58.8.1246.
- McCaffrey, R., A. I. Qamar, R. W. King, R. Wells, G. Khazaradze, C. A. Williams, C. W. Stevens, J. L. Vollick, and P. C. Zwick (2007), Fault locking, block rotation and crustal deformation in the Pacific Northwest, *Geophys. J. Int.*, 169, 1315–1340.
- McCaffrey, R., R. W. King, S. J. Payne, and M. Lancaster (2013), Active tectonics of northwestern U.S. inferred from GPS-derived surface velocities, *J. Geophys. Res. Solid Earth*, 118, 709–723, doi:10.1029/2012JB009473.
- Milne, G. A., J. L. Davis, J. X. Mitrovica, H.-G. Scherneck, J. M. Johansson, M. Vermeer, and H. Koivula (2001), Space-geodetic constraints on glacial isostatic adjustment in Fennoscandia, *Science*, 291, 2381, doi:10.1126/science.1057022.
- Montgomery-Brown, E. K., C. W. Wicks, P. F. Cervelli, J. O. Langbein, J. L. Svarc, D. R. Shelly, D. P. Hill, and M. Lisowski (2015), Renewed inflation of Long Valley Caldera, California (2011 to 2014), *Geophys. Res. Lett.*, 42, 5250–5257, doi:10.1002/2015GL064338.
- Oldow, J. S., J. W. Geissman, and D. F. Stockli (2008), Evolution and strain reorganization within Late Neogene structural stepovers linking the Central Walker Lane and Northern Eastern California Shear Zone, western Great Basin, *Int. Geology Rev.*, 50, 270–290, doi:10.2747/0020-6814.50.3.270.
- Parker, A. L., J. Biggs, and Z. Lu (2014), Investigating long-term subsidence at Medicine Lake Volcano, CA, using multitemporal InSAR, *Geophys. J. Int.*, 199, 844–859, doi:10.1093/gji/ggu304.
- Parker, A. L., J. Biggs, R. J. Walters, S. K. Ebmeier, T. J. Wright, N. A. Teanby, and Z. Lu (2015), Systematic assessment of atmospheric uncertainties for InSAR data at volcanic arcs using large-scale atmospheric models: Application to the Cascade volcanoes, United States, *Remote Sens. Environ.*, 170, 102–114.

- Parker, A. L., J. Biggs, and Z. Lu (2016), Time-scale and mechanism of subsidence at Lassen Volcanic Center, CA from InSAR, *J. Volc. Geothermal Res.*, **320**, 117–127.
- Peltier, W. R. (1998), Postglacial variations in the level of the sea: Implications for climate dynamics and solid-earth geophysics, *Rev. Geophys.*, **36**, 603–689, doi:10.1029/98RG02638.
- Poland, M., G. Bawden, M. Lisowski, and D. Dzurisin (2004), Newly discovered subsidence at Lassen Peak, southern Cascade Range, California, from InSAR and GPS, *Eos Trans. AGU*, **85**, Fall Meet. Suppl., Abstract G51A-0068.
- Poland, M., R. Bürgmann, D. Dzurisin, M. Lisowski, T. Masterlark, S. Owen, and J. Fink (2006), Constraints on the mechanism of long-term, steady subsidence at Medicine Lake volcano, Northern California, from GPS, leveling, and InSAR, *J. Volc. Geothermal Res.*, **150**, 55–78, doi:10.1016/j.volgeores.2005.07.007.
- Pollitz, F. F., C. Wicks, and W. Thatcher (2001), Mantle flow beneath a continental strike-slip fault: Postseismic deformation after the 1999 Hector Mine earthquake, *Science*, **293**, 1814–1818.
- Pollitz, F. F., P. McCrory, J. Svart, and J. Murray (2008), Dislocation models of interseismic deformation in the western United States, *J. Geophys. Res.*, **113**, B04413, doi:10.1029/2007JB005174.
- Renka, R. J. (1997), Algorithm 772: STRIPACK: Delaunay triangulation and Voronoi diagram on the surface of a sphere, *ACM Trans. Math. Soft.*, **23**(3), 416–434.
- Sella, G. F., S. Stein, T. H. Dixon, M. Craymer, T. S. James, S. Mazzotti, and R. K. Dokka (2007), Observation of glacial isostatic adjustment in “stable” North America with GPS, *Geophys. Res. Lett.*, **34**, L02306, doi:10.1029/2006GL027081.
- Sen, P. K. (1968), Estimates of the regression coefficient based on Kendall’s tau, *J. Am. Stat. Assoc.*, **63**, 1379–1389.
- Smith, K., G. M. Kent, D. P. von Seggern, N. Driscoll, and A. Eisses (2016), Evidence for Moho-lower crustal transition depth diking and rifting of the Sierra Nevada microplate, *Geophys. Res. Lett.*, doi:10.1002/2016GL070283.
- Smith-Konter, B. R., G. M. Thornton, and D. T. Sandwell (2014), Vertical crustal displacement due to interseismic deformation along the San Andreas Fault: Constraints from tide gauges, *Geophys. Res. Lett.*, **41**, 3793–3801, doi:10.1002/2014GL060091.
- Takeuchi, C. S., and Y. Fialko (2013), On the effects of thermally weakened ductile shear zones on postseismic deformation, *J. Geophys. Res. Solid Earth*, **118**, 6295–6310, doi:10.1029/2013JB010215.
- Tamisiea, M. E., and J. X. Mitrovica (2011), The moving boundaries of sea level change: Understanding the origins of geographic variability, *Oceanography*, **24**(2).
- Tape, C., P. Musé, M. Simons, D. Dong, and F. Webb (2009), Multiscale estimation of GPS velocity fields, *Geophys. J. Int.*, **179**, 945–971, doi:10.1111/j.1365-246X.2009.04337.x.
- Thatcher, W., and F. Pollitz (2008), Temporal evolution of continental lithospheric strength in actively deforming regions, *GSA Today*, **18**(4/5), doi:10.1130/GSAT01804-5A.1.
- Theil, H. (1950), A rank-invariant method of linear and polynomial regression analysis, *Indag. Math.*, **12**, 85–91.
- Thompson, G. A., and T. Parsons (2016), Vertical deformation associated with normal fault systems evolved over coseismic, postseismic, and multisismic periods, *J. Geophys. Res. Solid Earth*, **121**, 2153–2173, doi:10.1002/2015JB012240.
- Unruh, J., E. Hauksson, and C. H. Jones (2014), Internal deformation of the southern Sierra Nevada microplate associated with foundering lower lithosphere, California, *Geosphere*, **10**(1), 107–128, doi:10.1130/GES00936.1.
- Wdowinski, S., Y. Bock, J. Zhang, P. Fang, and J. Genrich (1997), Southern California permanent GPS geodetic array: Spatial filtering of daily positions for estimating coseismic and postseismic displacements induced by the 1992 Landers earthquake, *J. Geophys. Res.*, **102**(B8), 18,057–18,070, doi:10.1029/97JB01378.
- Wells, R. E., and R. W. Simpson (2001), Northward migration of the Cascadia forearc in the northwestern U.S. and implications for subduction deformation, *Earth Planets Space*, **53**, 275–283.
- Wesnousky, S. G. (2005), The San Andreas and Walker Lane fault systems, western North America: Transpression, transtension, cumulative slip and the structural evolution of a major transform plate boundary, *J. Struct. Geol.*, **27**, 1505–1512.
- Wessel, P., and W. H. F. Smith (1998), New, improved version of the Generic Mapping Tools released, *Eos Trans. AGU*, **79**, 579, doi:10.1029/98EO00426.
- Wicks, C. W., D. Dzurisin, S. Ingebretsen, W. Thatcher, Z. Lu, J. Iverson (2002), Magmatic activity beneath the quiescent Three Sisters volcanic center, central Oregon Cascade Range, USA, *Geophys. Res. Lett.*, **29**(7), 1122, doi:10.1029/2001GL014205.
- Williams, T. B., H. M. Kelsey, and J. T. Freymueller (2006), GPS-derived strain in northwestern California: Termination of the San Andreas fault system and convergence of the Sierra Nevada–Great Valley block contribute to southern Cascadia forearc contraction, *Tectonophysics*, **413**, 171–184, doi:10.1016/j.tecto.2005.10.047.
- Wöppelmann, G., and M. Marcos (2016), Vertical land motion as a key to understanding sea level change and variability, *Rev. Geophys.*, **54**, 64–92, doi:10.1002/2015RG000502.
- Zumberge, J. F., M. B. Heflin, D. C. Jefferson, M. M. Watkins, and F. H. Webb (1997), Precise point positioning for the efficient and robust analysis of GPS data from large networks, *J. Geophys. Res.*, **102**(B3), 5005–5017, doi:10.1029/96JB03860.